Volume: 4 Issue: 1 2023

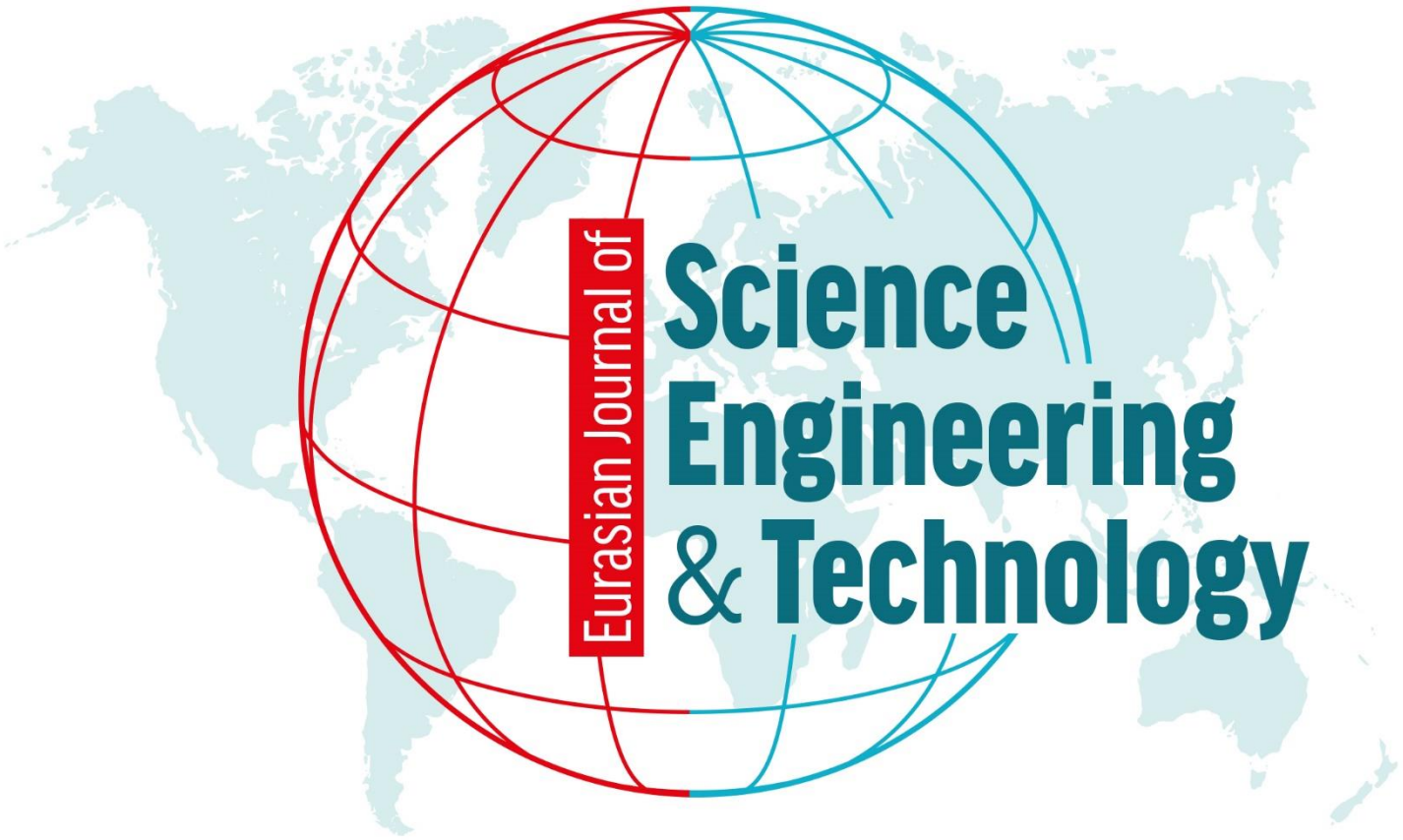

Eurasian Journal of Science Engineering and Technology

Editors

Editorial Board

Eurasian Journal of Science Engineering and Technology

Scientific Board

Eurasian Journal of Science Engineering and Technology

Correspondence Address

Niğde Ömer Halisdemir University
Eurasian Journal of Science Engineering and Technology Publishing Coordinatorship, 51240
Niğde/Türkiye

***E-mail*:** recep.zan@ohu.edu.tr
mbarut@ohu.edu.tr

***Web page*:** https://dergipark.org.tr/tr/pub/ejset

Publication information

The objective of Eurasian Journal of Science Engineering and Technology (EJSET) is to provide an academic environment for researchers in various fields of science and engineering and for the publication and dissemination of high-quality research results in the fields of science, applied science, engineering, architecture, agricultural science and technology.

Eurasian Journal of Science Engineering and Technology

CONTENTS/*İÇİNDEKİLER*

Eurasian Journal of Science Engineering and Technology

Research Article

ALTERNATIVE NUMERICAL SIMULATION APPROACH FOR OBTAINING FLC/FLD

Serap DİKMENLİ [1,*]

[1] *Altinay Robot Teknolojileri San. ve Tic. A.S., Istanbul Anadolu Yakasi O. S. B. Aydinli Mh. 2. Sanayi Cd. No.22, Tuzla 34956 İstanbul Türkiye*

ABSTRACT

To be able to predict the forming behavior of sheet metal parts by simulation, it is necessary to determine the FLD[1] (Forming Limit Diagram) curves of the sheet material that is subjected to bending, hemming, deep drawing, progressive forming, embossing, hydro-forming processes. To determine such curves, the usual practice is to carry out a series of experiments that need to be repeated many times, and therefore it takes a long time to finalize them [1], [2], [3], [4], [5], [6]. Not to mention undertaken experiments are very detailed and need tedious and careful work has to be done such as screen printing on the material and doing simultaneous optical measurements during the experiments. Indeed, a fully equipped laboratory and qualified lab personnel are required for such experiments which may not be easily found. When it's found, there is usually six months to a year, queue to conduct such experiments.

Because of these difficulties, many academic institutions and manufacturing sites develop their in-house test equipment if funding is available. If not, it is dependent on research whether it comes to an end or whether it can continue without it.

An alternative method developed for extracting FLD/FLC curves is using today's state-of-the-art simulation technology. This method requires two main inputs;

a) Tensile test of the material
b) An explicit solver

The scope of this paper is to detail this method such that the findings in this document can be reproduced when the mentioned requirements are satisfied. Therefore, all data used in charts, a high-resolution image, and a sample Abaqus input file are provided as supplemental data [7].

The results from the simulations of FLD/FLC were compared to published literature [13] [14] to confirm their compliance with experiments. The comparison showed good results and demonstrates that expensive and time-consuming FLD/FLC experiments are not necessary when the mentioned requirements are met.

Keywords: FLD, FLC, Sheet Metal, Forming, Bending, Hemming, Forming Limit Diagram, Forming Limit Curve

1. INTRODUCTION

FLD/FLC curves of the sheet metal that will be subjected to any forming process should be determined for the necking and/or cracks that may occur during the forming process in numerical analysis/simulations. To do that, it is necessary to carry out a series of experiments those need to be repeated many times and take a long time. Detailed and very careful work should be carried out, which includes screen printing on the material and using optical measuring devices during the experiment [1]. It may be because this should have been done in the Covid-19 pandemic timeline; there was no single laboratory that can perform this experiment in Turkey. To find the FLD curves of the materials, there were three options;

a) Developing the necessary experimental equipment in-house.
b) Because of the force major (Pandemic), this requirement will be ignored and surpassed.
c) Some other practical and versatile alternatives should be developed.

Fortunately, as a result of a long investigation, research, [8]-[11] and trial and error, it is discovered that extracting the FLD curve of materials is possible with a quasi-static explicit solver and tensile test results of the material.

This paper details how these curves were obtained in such a way that the reader should need no other than the requirements, references, and method stated in this paper. Also, since it took one and a half months man-hour time to find the right method for a similar need, using the information and data provided in this article can at least save that much research time for the reader.

[1] Also known as FLC (Forming Limit Curve)

* Corresponding author, e-mail: serap.dikmenli@gmail.com (S. Dikmenli)
Recieved: 30.11.2022 Accepted: 15.03.2023
doi: 10.55696/ejset.1212311

2. STRESS-STRAIN CURVE

The stress-strain curve obtained as a result of the tensile tests performed on the material (according to [8]) in determining the basic mechanical elastic-plastic material model properties gives us the most basic information at room temperature. All the tensile test specimens are prepared 90º in Rolling Direction, which is known to be the weakest material direction for tensile tests.

Ramberg-Osgood Equation

The stress-strain curve of the material can be obtained as a result of multiple tensile tests. As an alternative method, if the elasticity (Young) modulus, stress, and strain values at the yield and ultimate points of the material are known, the stress-strain curve of the material can be established with the "Ramberg-Osgood" relation [9]. The "Ramberg-Osgood" relation tries to simulate the behavior of the material in both the elastic and plastic regions. The total strain relation on both regions as a function of stress can be expressed as;

$$\varepsilon = \frac{\sigma}{E} + 0.002\left(\frac{\sigma}{\sigma_y}\right)^{1/n} \tag{1}$$

Where, ε strain, σ stress, E elasticity modulus, σ_y tensile yield stress and n known as strain hardening exponent of material which can be obtained from;

$$n = \frac{\log\left(\sigma_u/\sigma_y\right)}{\log\left(\varepsilon_f/_{0.002}\right)} \tag{2}$$

Where, $\sigma_u$is the ultimate stress value of the material and ε_f is known as plastic strain and can be calculated from;

$$\varepsilon_f = \varepsilon_u - \frac{\sigma_u}{E} \tag{3}$$

Where, ε_u is the ultimate strain value of the material.

All the above-mentioned values (σ_u, σ_y, E and ε_u) can be either obtained from material tables or derived from material tensile test results. As an example for Aluminum 6061-T6 material, the convergence of "Ramberg-Osgood" & tensile test results can be compared as follows;

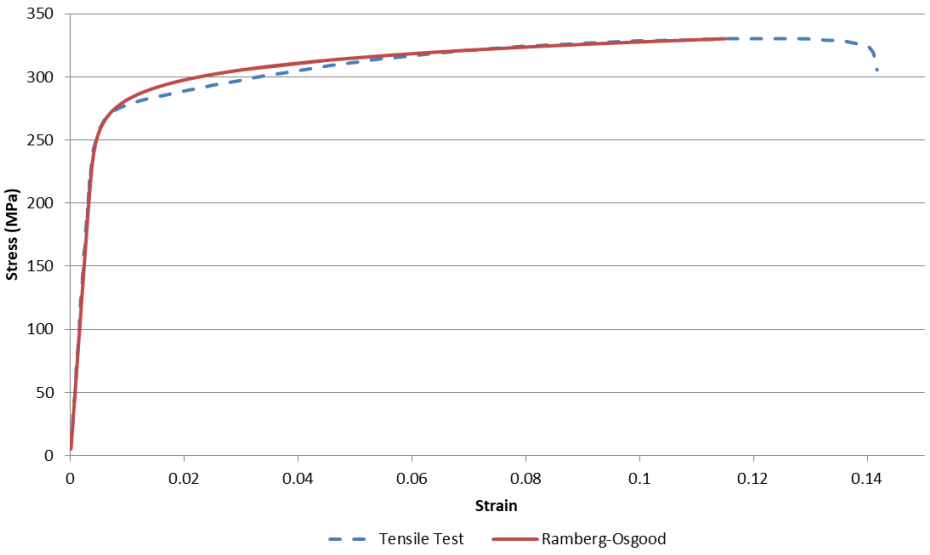

Figure 1. Comparison of Ramberg-Osgood Equation and tensile test results

As can be seen from

Figure **1**, although the Ramberg-Osgood relation converges quite well to the tensile test in the elastic and near-tensile plastic region, it can produce results that diverge significantly, at least for aluminum material, right after the elastic region. Therefore, directly using tensile test results for the simulation will produce more reliable and realistic results.

3. TRUE STRESS – STRAIN CURVE

The stress-strain curve obtained as a result of the tensile tests is called the engineering stress-strain curve. However, simulation software such as Finite Elements uses the "True" stress-strain curve, which takes into account the change in the cross-sectional area of the specimen during the tensile test.

The relationship between the Engineering and True Stress-Strain curve is defined [10] by the following formulas;

$$\sigma_t = \sigma_e(1 + \varepsilon) \tag{4}$$

$$\epsilon = \ln(1 + \varepsilon) \tag{5}$$

Where, σ_t and ϵ are true stress and strain, and σ_e and ε are engineering stress and strain values.

Accordingly, the engineering and true stress-strain curves of an experiment performed on Aluminum 6061-T6 material are as follows;

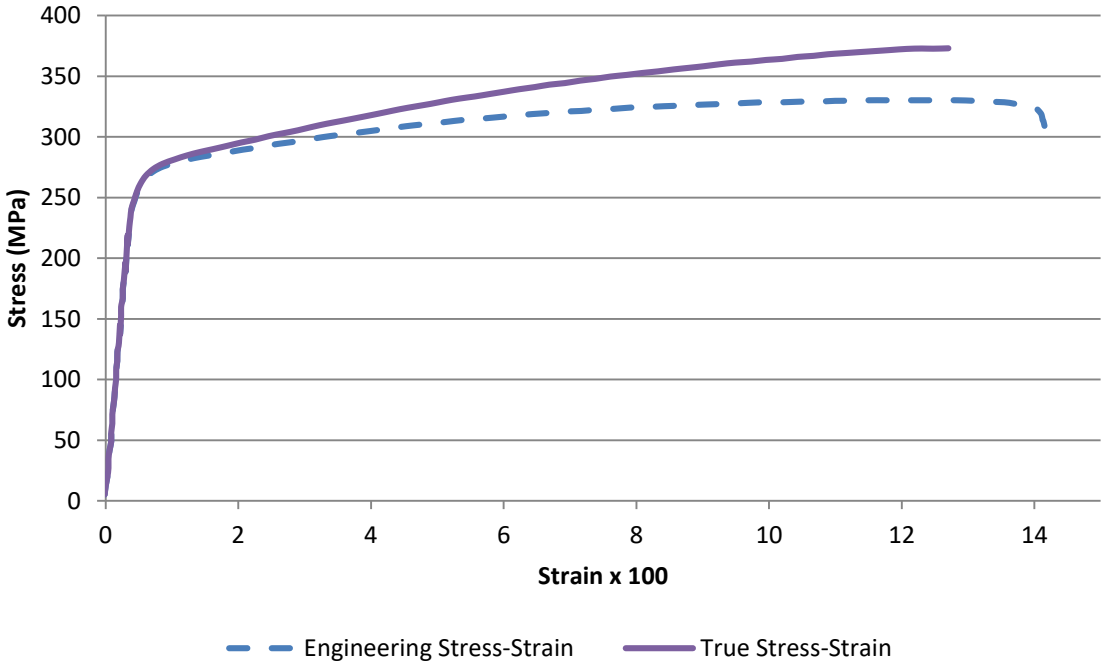

Figure 2. Comparison of engineering and true stress-strain curves of AL6061-T6

Engineering curves obtained as a result of tensile tests were converted into true curves which are used in all simulation studies.

4. OBTAINING FLD/FLC CURVE OF A MATERIAL

There are many sources, such as reference [1], describing how the Forming Limit Diagram (FLD) is experimentally derived. There are [2], [3], [4], [5] and [6] standards related to the derivation of this curve, and among these standards, the "Nakajima" test defined in the standard [3] was used as the base reference in finding the FLD curves in this document. The mold geometry definition for the Nakajima test is as shown in the following Figure 3;

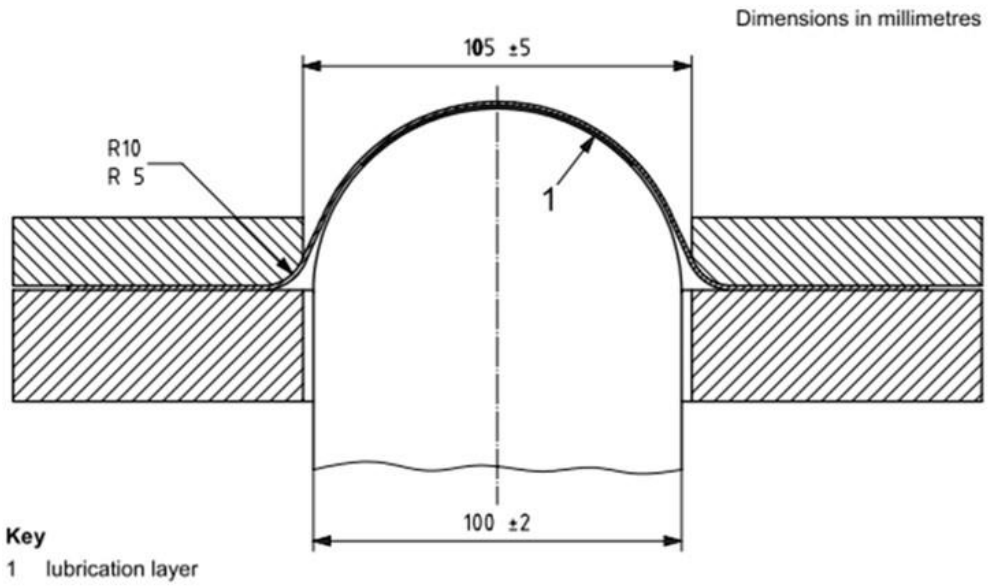

Figure 3. Die cross-section used in Nakajima Test

In standard [3], PTFE material is used as the sliding surface, and therefore, the dynamic friction coefficient is assumed to be 0.15 for both aluminum and steel parts. It is also one of the conclusions of reference [11] that such an assumption will produce correct results.

According to the standard, the speed of the punch should be 1.5 mm/s. The friction coefficients were accepted as shown in the following Table 1;

Table 1. Friction coefficients

	Steel-Steel	**Steel-Aluminum**	**Aluminum-Aluminum**
Static	0.8	0.45	1.35
Dynamic	0.42	0.47	1.4

To achieve different stress-strain states, separate geometries are used to find each point on the FLD curve. The sample sheet metal part geometries that can be selected by the Nakajima test are as Shown in the following Figure 4;

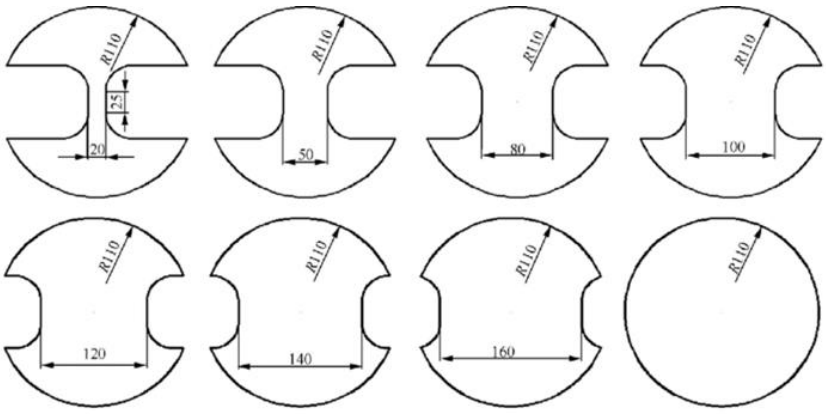

Figure 4. Part geometries

The properties of the following materials were used in the simulation studies to create FLD curves for three different materials are shown in the following Table 2;

Table 2. Main material properties

	AL 6061-T6	AL 6016-T4	CR180BH
Density (g/cm3)	2.70	2.70	7.00
Elasticity Modulus (GPa)	62.50	66.00	209.70
Poisson's Ratio	0.33	0.33	0.30

Above in

Figure **2**, the true stress-strain curve of AL6061-T6 material is given. Likewise, the true stress-strain curve for both AL6016-T4 and CR180BH materials is given below in the following Figure 5 and Figure 6. In simulation studies, the true stress-strain values used in the plastic region with a negative offset in strain such that strain at the yield point is accepted as its 0 (zero) value.

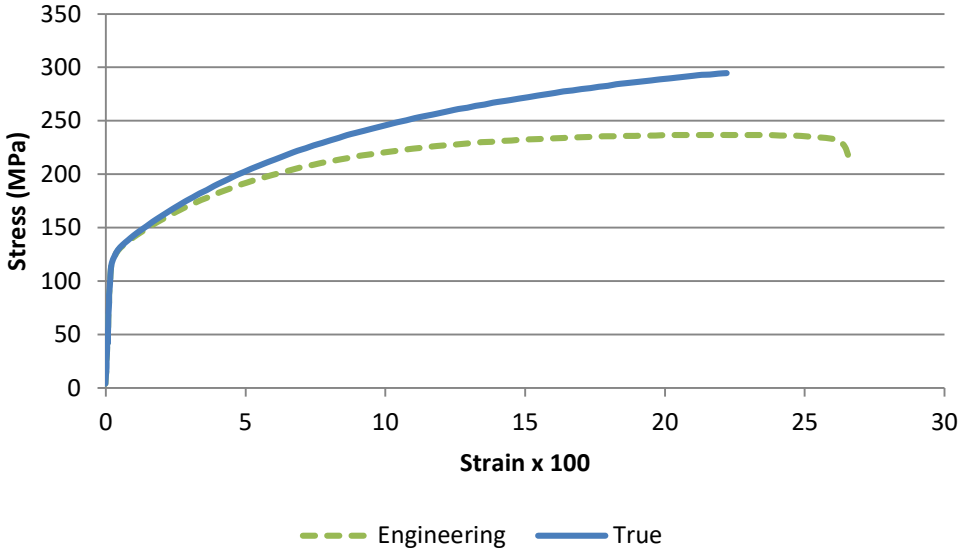

Figure 5. Comparison of engineering and true stress-strain curves of AL6016-T4

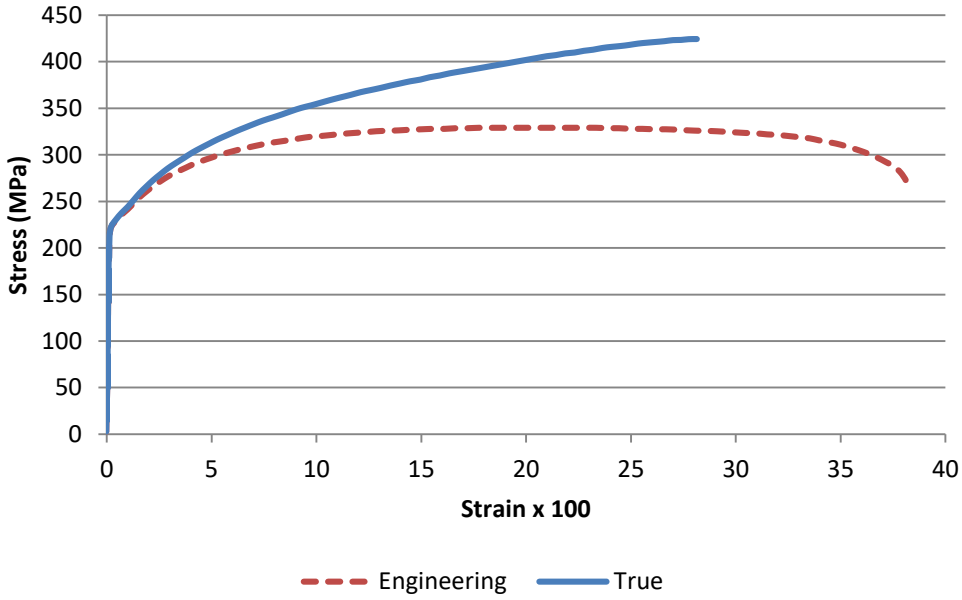

Figure 6. Comparison of engineering and true stress-strain curves of CR180BH

5. DETERMINATION OF MINOR AND MAJOR STRAINS

In physical tests, major and minor strains occurring immediately at the crack initiation are taken into account. Only a single major and a single minor strain point can be extracted from each test done on different geometry. It is known that the minor and major strains at the crack initiation are the ones that we are seeking after.

To detect the crack initiation, the reaction force graph in real experiments was examined in finding the FLD curve. The point where the counter force applied to the system by the geometry (reaction force) peaks and starts to decrease is accepted as the beginning of crack initiation and the plastic major and minor strains at this point are determined [11]. By using this method, it was observed that the obtained minor-major strain curve did not produce realistic results, especially for the positive minor strain values which are near 0 (zero).

Instead, it has been discovered that realistic results could be achieved in the FLD inference made by considering the starting points of the sudden change in the major-minor strain values on the FEM element that has the utmost deformation (

Figure **7**).

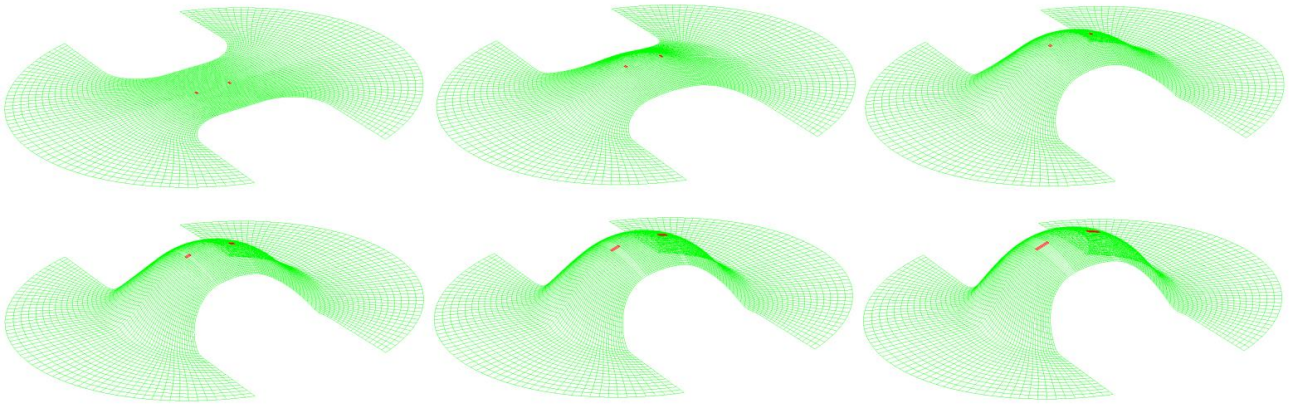

Figure 7. FEM element shown as red is subject to the utmost deformation on the Nakajima FEM test simulation

On above mentioned the most deformed FEM element of the test specimen, major & minor strain values are obtained, and their change is plotted as shown in Figure 8. Below, it has been tried to show where these crucial sudden changes or also known as fracture points are in the graph;

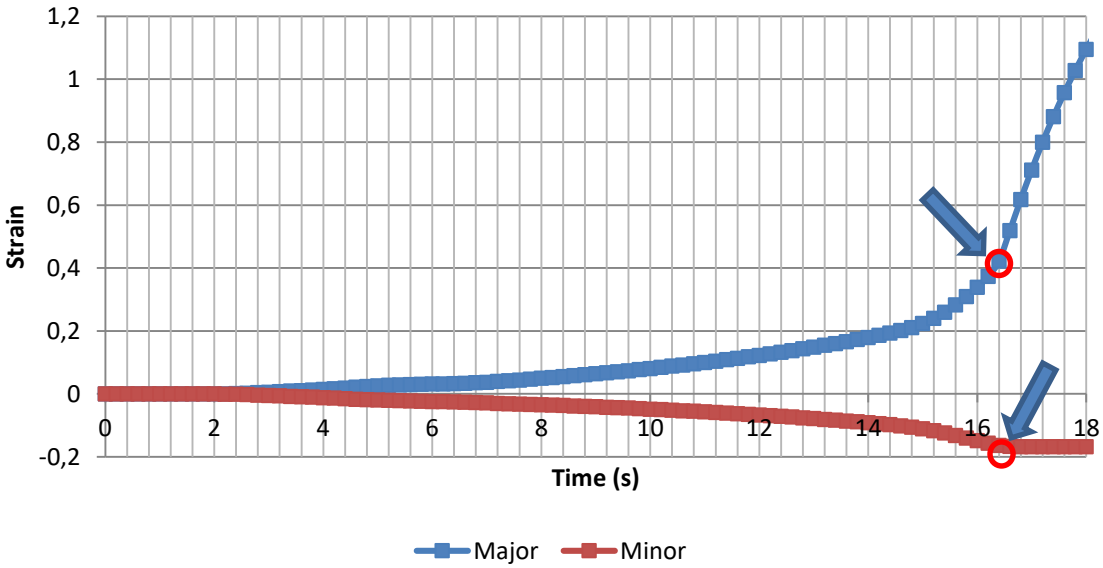

Figure 8. Major-minor plastic strain change graph at the integration point of the finite element exposed to the maximum deformation and the points where the values taken for the FLD curve are shown in this graph.

The points found in the above approach can also be perceived as values that occur at the beginning of the maximum tangent on the major strain curve and the beginning of the minimum tangent on the minor strain curve.

It is later found that the method introduced in this paper is almost identical to [12] which proposes the maximum strain acceleration at the most strained locations as the fracture indicator.

6. FLD/FLC CURVES

In a nutshell, the forming limit curves are determined through applying strains to metal samples in tests until a crack appears. Samples are marked with a grid pattern and the strains are calculated based on the measurement of the grid before and after deformation. The FLD is generated from the calculated major and minor strains for different strain states.

Tensile test and FLD/FLC simulation studies are conveyed on three different sheet metal materials in the scope of this report. These are;

- Aluminum 6061-T6
- Aluminum 6016-T4
- CR180BH

Their corresponding simulation results shown in the following Figure 9, Figure 10, and Figure 11 respectively;

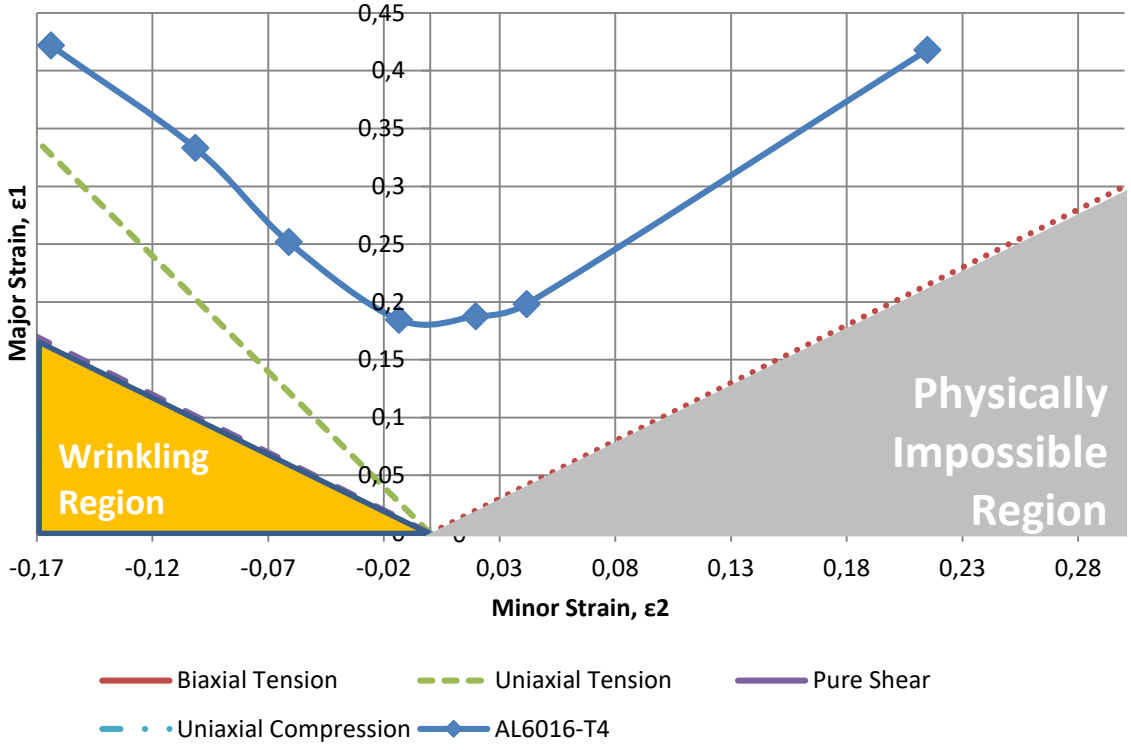

Figure 9. FLD Curve of AL6016-T4 sheet-metal material as a result of numerical simulations

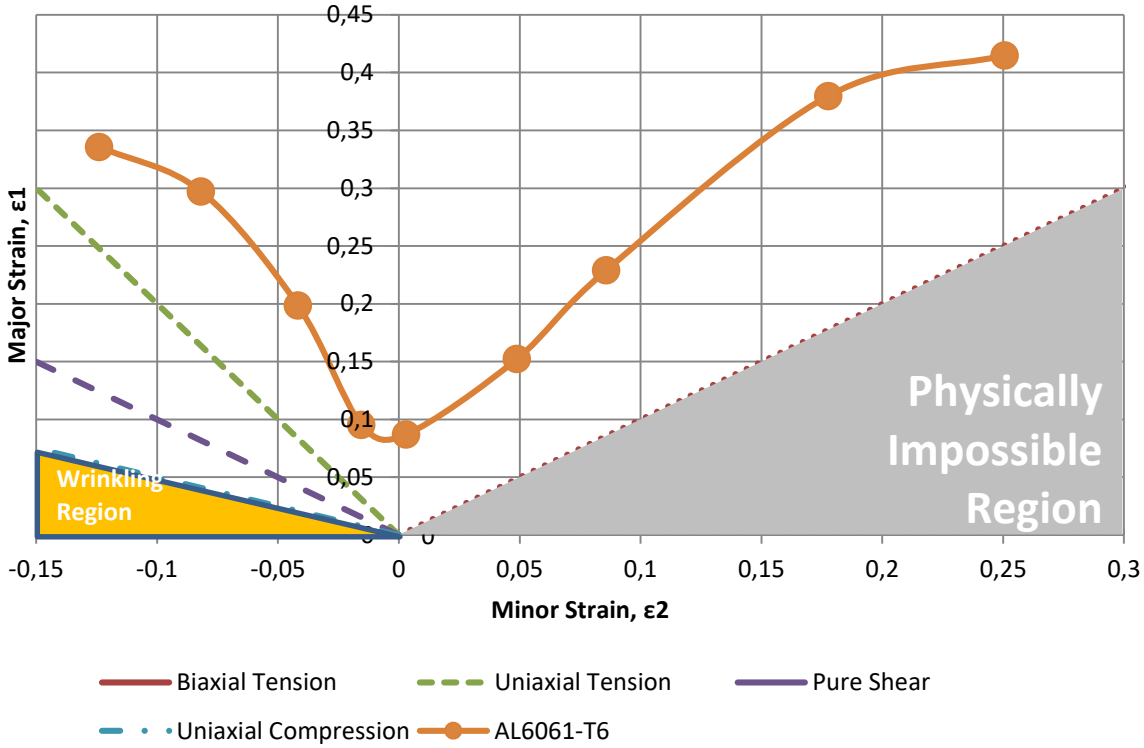

Figure 10. FLD Curve of AL6061-T6 sheet-metal material as a result of numerical simulations

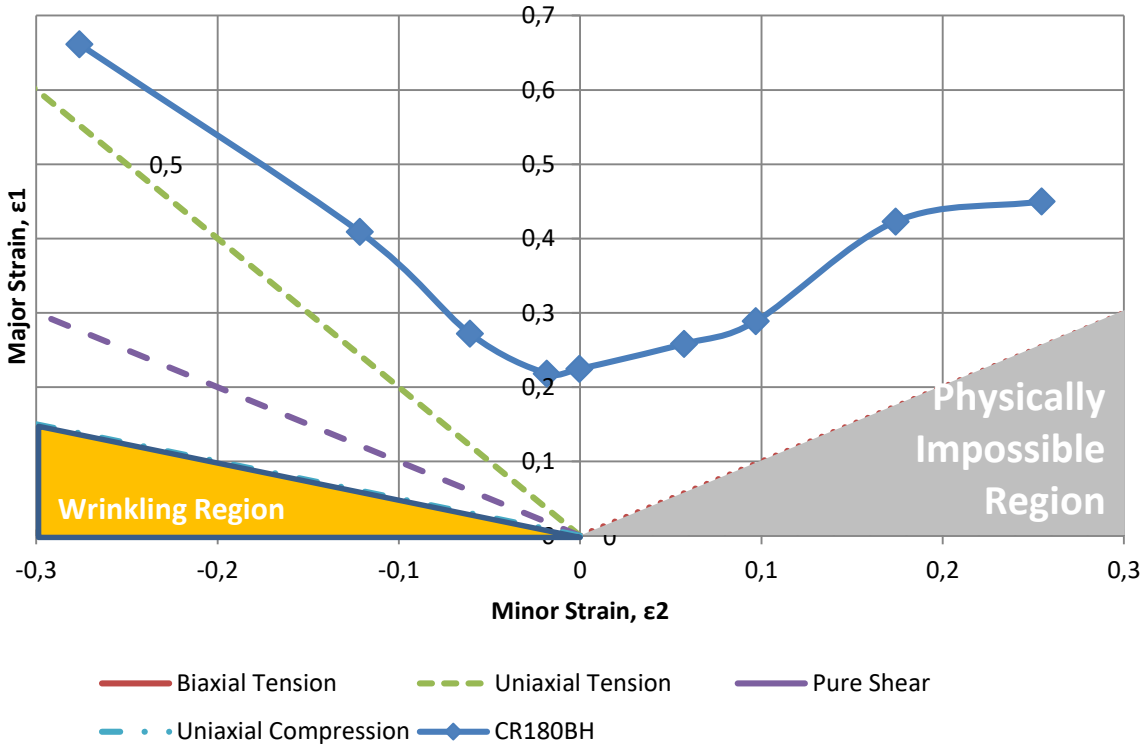

Figure 11. FLD Curve of CR180BH sheet-metal material as a result of numerical simulations

7. CONCLUSION

The FLD curve results obtained are quite satisfactory as they are similar to the results found in internet resources for the materials CR180BH [13] and AL6061-T6 [14].

The curves found for the detection and comparison of crack regions during sheet-metal forming processes can be used in physical testing, in comparison of simulation studies, and, if necessary, in simulation convergence studies with the test results.

The outcome of this study should not be considered as the total replacement of the very tedious and expensive physical test method of finding FLD/FLC curves but can be considered as the economical alternative method instead. This outcome is an important achievement by itself, not to mention alternative physical methods may be out of the scope of most SMEs world-wide if such input curves are required for the extended studies.

SIMILARTY RATE: 2 %

REFERENCES

[1] P.E. Smith; D. Lee, Determination of Forming Limits for Aluminum Alloys, SAE Technical Paper 982375, 1998

[2] ISO 12004-1, Metallic material - Sheet and Strip - Determination of forming-limit curves. Part 1: Measurement and application of forming limit diagrams in press shop, 2008.

[3] ISO 12004-2, Metallic material - Sheet and Strip - Determination of forming-limit curves. Part 2: Determination of forming-limit curves in the laboratory, 2008.

[4] ASTM E2218-02, 2008, "Standard Test Method for Determining Forming Limit Curves," Annual Book of ASTM Standards, Vol. 03.01, ASTM International, West Conshohocken, PA.

[5] ASTM E643, Standard Test Method for Ball Punch Deformation of Metallic Sheet Material, 2009.

[6] ISO 20482, Metallic Materials - Sheet and strip - Erichsen cupping test, 2003.

[7] S. Dikmenli, Alternative Numerical Simulation Approach for Obtaining FLC/FLD - Supplementary Data (https://data.mendeley.com/datasets/4wg9nkz8b6), Mendeley Data, V1, doi: 10.17632/4wg9nkz8b6.1, 2022

[8] ISO 6892-1, Metallic materials — Tensile testing. Part 1: Method of test at room temperature, 2019

[9] Mechanical Properties of Materials (https://mechanicalc.com/reference/mechanical-properties-of-materials#stress-strain-approx), MechaniCalc Inc., November, 23th 2022.

[10] S. Korkut, Serdar, Gerilme-Gerinim (Stress-Strain) Eğrisi (https://www.serdarkorkut.com/2017/05/09/gerilme-gerinim-stress-strain-egrisi/), November, 23th 2022.

[11] W. Yuan, M. Wan, X. Wu, "Prediction of Forming Limit Curves for 2021 Aluminum Alloy", *Procedia Engineering*, 207, 544-549, 2017.

[12] D. Lumelskyj, J. Rojek, L. Lazarescu, D. Banabic, "Determination of forming limit curve by finite element method Simulations", *Procedia Manufacturing*, 27, 78-82, 2019

[13] Bake hardening steels (https://automotive.arcelormittal.com/products/flat/HYTSS/BH), ArcelorMittal, November, 23th 2022.

[14] F. Djavanroodi, A. Derogar, "Experimental and numerical evaluation of forming limit diagram for Ti6Al4V titanium and Al6061-T6 aluminum alloys sheets", *Materials and Design*, vol 31, pp 4866–4875, 2010.

Eurasian Journal of Science Engineering and Technology

Research

INFLUENCE OF HEATING RATE ON THE STRUCTURAL AND OPTICAL PROPERTIES OF SILVER AND GERMANIUM CO-DOPED CZTS THIN FILM

Yavuz ATASOY[1*], Ali ÇİRİŞ[2], Mehmet Ali OLĞAR[3]

[1,2,3] *Nigde Omer Halisdemir University, Nanotechnology Research Center, 51240, Nigde, Türkiye*
[1]*Niğde Ömer Halisdemir University, Niğde Zübeyde Hanım Health Services Vocational High School, 51240 Nigde, Türkiye*
[3]*Nigde Omer Halisdemir University, Department of Physics, 51240, Nigde, Türkiye*

ABSTRACT

The effect of heating rate on the structural and optical properties of Ag+Ge co-doped CZTS thin film were investigated and compared with the undoped CZTS sample. The undoped and Ag+Ge co-doped CZTS samples obtained by two-stage technique consisting of the sequential deposition of the precursor stacks by sputtering systemand sulfurization of these layers at elevated temperature in the RTP system by employing heating rate of 1°C/s, 2°C/s and 3°C/s. Ag and Ge co-doped precursor stack as well as undoped stack demonstrated Cu-poor, Zn-rich composition. In addition, the dopant ratio of the Ag+Ge co-doped stack was close to the targeted content considering to EDS measurement. Regardless of the employed heating rate or the doping process, all of the samples crystallized in a kesterite structure. However, it was confirmed by XRD measurements that high heating rates caused phase separation in kesterite phase formation. On the other hand, The Raman peaks assigned to Cu-vacancy and Cu_{Zn} antisite defects formation inhibited with incorporating Ag and Ge into the CZTS structure. Ag and Ge co-doped CZTS sample produced with a heating ramp rate of 1°C/s showed better structural and optical results among them.

Keywords: Ag and Ge co-doping, CZTS Thin Film, Sputtering, Rapid Thermal Processing, Heating Rate

1. INTRODUCTION

The Cu-based kesterite compounds such as Cu_2ZnSnS_4, (CZTS), $Cu_2ZnSnSe_4$ (CZTSe) $Cu_2ZnSn(S,Se)_4$ (CZTSSe) are shown as alternatives to the absorber layers used in the mature thin-film-based solar cell technologies ($CuIn_{1-x}Ga_x(S,Se)_2$ (CIGS) and CdTe), since kesterite materials contain earth abundant and non-toxic elements. Moreover, kesterite thin films also demonstrate similar characteristics to those they are compared to. i.e. having high absorption coefficient (10^4-10^5 cm^{-1}), closer ideal direct band gap (1.5 eV) and p-type conductivity which make them an appropriate candidate for photovoltaic applications[1, 2]. However, it is known that the experimental photo conversion efficiency obtained from CZTSSe-based solar cells (~13%) is lower than the theoretical value (~ 33%), as well as CIGS (23.1%) and CdTe (22.9%) solar cells [3, 4]. This difference is mostly attributed to the low Voc [5]. The formation of high acceptor defects concentration such as V_{Cu} and Cu_{Zn} due to Cu-Zn disorder that occur during the formation of the kesterite structure is referred to the Voc deficiency [6]. On the other hand, deep defect levels originating from the formation of unstable Sn^{+2} ions have been widely reported as a reason of low efficiency of the CZTSSe devices [7].

To overcome these defects related to issues mentioned above, alloying of kesterite material is one of the main approach that used. In this context, the cation replacement of copper (Cu) with silver (Ag) or tin (Sn) with germanium (Ge) in CZTSSe have been mostly reported in the literature. For example, it has been reported that partial replacement of Ag with Cu decreases the V_{cu} and Cu_{Zn} defects, induces better surface morphology with a larger grains and controls the thickness of the MoS_2 [8] . Such improvements in the structure of the films contributes to enhance the cell efficiency. Besides, it has also been revealed by some reported studies that, the concentration of defects in the structure decreased, the crystalline quality improved and grain boundary recombination decreased by Ge doping in CZTSSe thin film [7]. Apart from these, there have been limited amount of work focused on double cation substitution in CZTSSe structures to simultaneously cope with the Cu-Zn disorder and Sn-related problems [9, 10]. In addition, it has been revealed that Ag and Li co-doping strategy improves performance of CZTSe based thin film solar cell by reducing poor electrical conductivity [11].

In this study, we reported Ag and Ge co-doped CZTS thin films prepared by Rapid Thermal Processing (RTP) method for the first time. In order to find the optimum growth process, the effect of heating rate on the structural and optical properties of Ag and Ge co-doped CZTS thin films investigated. For comparison, undoped CZTS thin films were also produced.

* Corresponding author, e-mail: yavuzatasoy@ohu.edu.tr (Y.Atasoy)
Recieved: 10.05.2023 Accepted: 25.05.2023
doi: 10.55696/ejset.1295349

2. MATERIAL AND METHOD

Undoped (CZTS) and Ag-Ge co-doped CZTS (ACZGTS) thin films were grown by the two-stage method. First of all, precursor films were constructed on Soda-Lime Glass (SLG) substrates by DC and RF magnetron sputtering system employing high purity ZnS (5N), Cu (5N), Sn (5N), Ag (4N) and Ge (5N) sputter targets. Then, the precursor stacks were annealed under sulfur atmosphere using the RTP method with different heating rates to form Ag and Ge co-doped CZTS kesterite structure. For deposition of precursor stacks of undoped and Ag+Ge co-doped samples, SLG substrates were cleaned through standard procedure, were placed into the sputtering chamber, and then SLG/Mo/ZnS/Cu/Sn/Cu and SLG/Mo/ZnS/CuSn/Cu/Ag/Ge stacks were obtained with using high purity sputtering targets, respectively. The SLG/Mo/ZnS/CuSn/Cu stack was used in the present study due to promising results were obtained using this structure in our previous study [12]. Finally, the stacks were sulfurized at 550°C for 1 min by using different heating rates of 1°C/s, 2°C/s and 3°C/s. It is well-known that the RTP is more attractive method for large scale production due to higher throughput and low energy consumption compared to Conventional Thermal Processing (CTP) method and it is also more favorable due to the fact that the shorter annealing time prevent the decomposition reactions and elemental loss in CZTS compounds [13]. The detailed information about the deposition process can be found elsewhere [9, 14].

The chemical composition of the precursor stacks were investigated by Energy Dispersive X-ray Spectroscopy measurements (EDS). The polycrystalline properties of the thin films were determined by X-ray diffraction (XRD) and Raman spectroscopy (excitation wavelength of 633 nm) methods. The optical properties of the samples were studied by optical transmission measurement.

3. RESULTS AND DISCUSSION

The chemical composition of the undoped and Ag+Ge co-doped precursor layers was given in Table 1. Two stacks were found to be Cu-poor (Cu+Ag/Zn+Ge+Sn) and Zn-rich (Zn/Ge+Sn) composition with the ratio of about 0.9 and over 1.30, respectively. The Cu-poor and Zn-rich chemical composition is desired property in CZTS-based thin film solar cell applications since such composition contributes to form Cu vacancies (V_{Cu}) and Cu_{Zn} anti-site defects, which strengths the p-type conductivity, improves the Cu and Zn cation ordering in the lattice, and enhances the separation of photo-generated electron-hole pairs [15].

According to the doping concentration of the Ag and Ge co-doped stack, it was seen that Ag and Ge ratio was about 6% and 11%, respectively that was close to the targeted dopants ratio (10%). Regardless of the deposition process, the chemical compositions of the samples demonstrate that the doped stack has been successfully formed even if it contained six different elements.

Table 1. EDS results of undoped and Ag+Ge co-doped precursor stacks

Precursor	Atomic Compositions (%)						Atomic Ratios			
	Cu	Ag	Zn	Sn	Ge	S	$\frac{(Cu+Ag)}{(Zn+Ge+Sn)}$	$\frac{Zn}{(Ge+Sn)}$	$\frac{Ag}{(Ag+Cu)}$	$\frac{Ge}{(Ge+Sn)}$
Undoped	36.0	-	24.2	14.9	-	24.9	0.92	1.60	-	-
Ag and Ge co-doped	31.4	1.7	22.4	14.5	1.9	28.1	0.85	1.36	0.06	0.11

XRD patterns of CZTS and ACZGTS thin films produced by sulfurization of undoped SLG/ZnS/CuSn/Cu and co-doped SLG/ZnS/CuSn/Cu/Ag/Ge and structures for 1 min at 550°C are given in Figure 1(a-b), respectively. It was observed in XRD patterns of the samples that irrespective of dopants and heating rate crystallized in the kesterite structure. Dominant diffraction peaks of the samples in the XRD patterns are at angles of around 2θ= 28.45°, 47.50°, and 56.30° which belong to the (112), (220/204) and (312/116) crystal planes of the kesterite CZTS phase, respectively (JCPDS 00-26-0575). Apart from these peaks, the trace of low-intensity characteristic peaks that occur in the crystal planes of (002), (200), (008) and (332) that are also attributed to the kesterite phase. Extended patterns in the range of 2θ= 28-29° correspond to the (112)-peaks of the XRD patterns demonstrated in Figure 1(a-b) are given in Figure 2(a-b). It was determined that the (112) peak positions of the CZTS samples did not change with the increasing heating rate as well as the Ag+Ge co-doped CZTS samples ones. Vegard's law states that

there is a linear relationship between the crystal lattice constant and the concentrations of the elements involved in the structure [16]. This shifts in the XRD peak position inversely proportional to the ionic radius of the dopant atom that replaces the host atom in the lattice. In our case, it is expected that the Bragg angle, 2θ, shifts to lower angle by the replacement of Cu with Ag (larger radius) into the CZTS structure, while it shifts to a higher angle by the replacement of Sn with Ge (smaller radius) [17, 18]. Considering the differences between the ionic radii of the Ag and Ge contributions in the lattice and the atomic ratios in the stack of the samples produced at 550°C, it was determined that the shifts in the peak position compensated each other and presented the same diffraction pattern.

When the effects of the heating rate on the XRD pattern of undoped CZTS thin films were examined closely, it was concluded that the value of the full width at the half-maximum as known an indicator of crystallization degree decreased (0.170°➞ 0.155° ➞ 0.150°) with the increasing heating rate (1°C/s ➞ 2°C/s ➞ 3°C/s). Although the increase in the heating rate improved the crystal quality, it was determined that there was a relative decrease in the (112) peak intensity of these samples and a shoulder peak was formed at around 2θ= 29.55°, which corresponds to the ZnS phase (JCPDS 00-002-0564). In contrast, the Ag and Ge co-doped CZTS thin film produced at 1°C/s with a half-maximum width of 0.17° shown the best crystal quality among them. As a result of XRD measurements, the optimum heating rate for the growth of undoped and Ag+Ge co-doped CZTS thin films is 1°C/s.

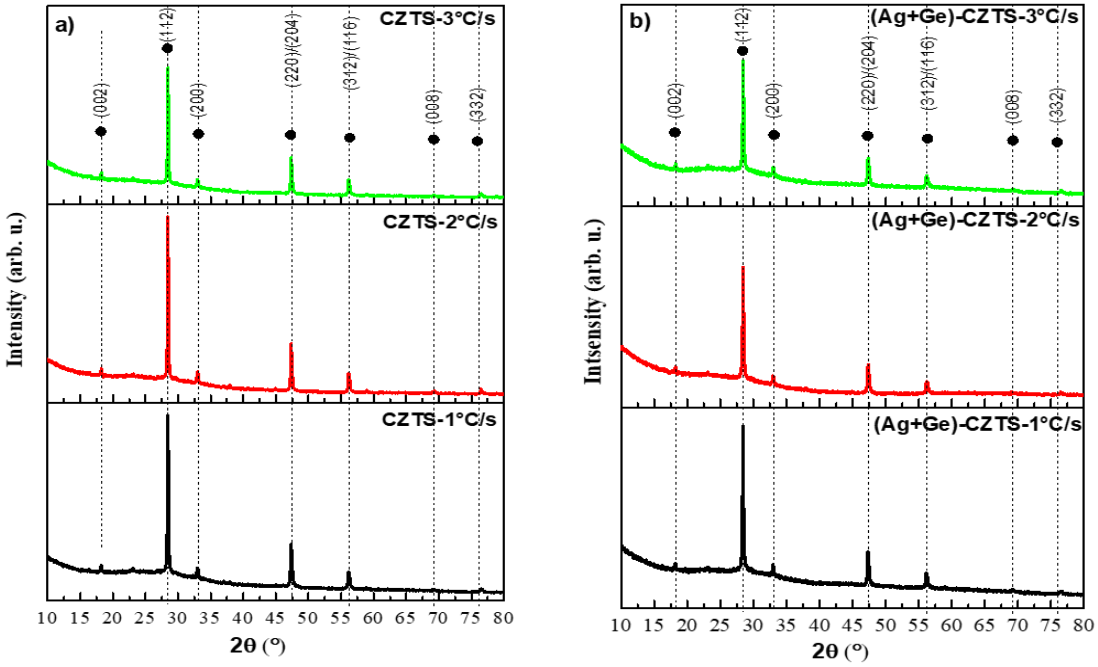

Figure 1. XRD spectra of a) undoped, b) Ag+Ge co-doped CZTS thin films formed with various heating rates.

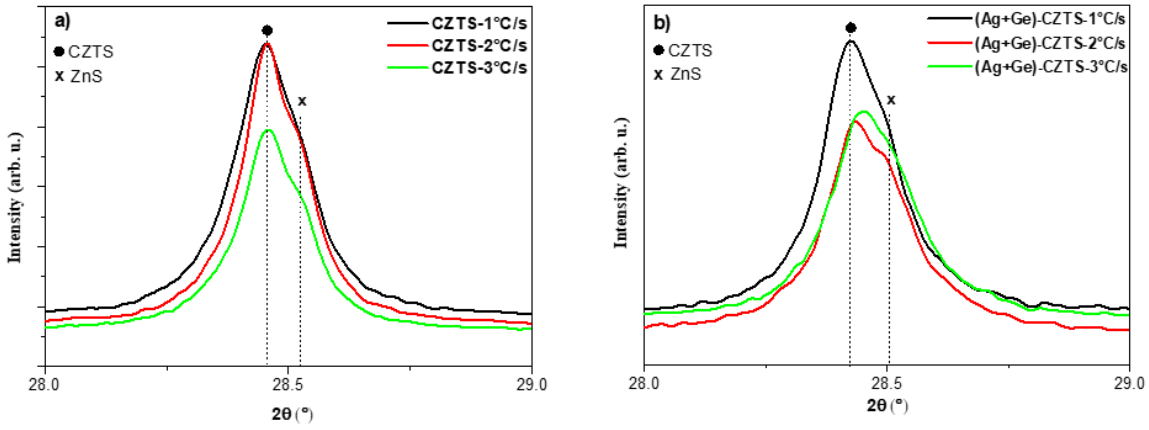

Figure 2. Extended XRD patterns of a) undoped, b) Ag+Ge co-doped CZTS thin films formed with various heating rates.

Raman spectra of undoped and Ag+Ge co-doped CZTS samples produced by employing various heating rates are shown in Figure 3 (a-b). In Raman spectra taken in the range of 200-500 cm^{-1}, a dominant peak at about 336 cm^{-1} (corresponds to the A1 mode of the kesterite structure) occurred regardless of the heating rate for all of the samples [19]. For undoped CZTS samples, the peaks formed at 264, 286 and 366 cm^{-1} of the kesterite phase are marked in the figure and are in accordance with the previous studies [20, 21]. In addition to these, along with a peak formed at 304 cm^{-1} which is attributed to the CTS phase, the Raman peaks at 287 and 367 cm^{-1} associated with V_{cu} and Cu_{Zn} defects appeared, respectively [22, 23]. Besides, although ZnS phase was observed in the XRD pattern of the samples, it was not detected with Raman spectroscopy measurement due to the insufficient energy of the excitation wavelength of the laser. When the Raman spectra of Ag and Ge co-doped CZTS film were examined, it was determined that the Raman modes of the kesterite phase varied with the heating rate, except for the main peak around 336 cm^{-1}. Apart from this, Ag-S or Ge-S related secondary phases did not emerged, depending on the dopants. The Raman peaks associated to V_{cu} and Cu_{Zn} defects concentration decreased by introducing Ag and Ge into the structure. Also, there was no change in the main peak position. However, similar to the XRD results, it is expected that there will be shifts in the main peak position (336 cm^{-1}) with introducing Ag and Ge into the structure separately. It is thought that the Raman peak position of the A1 mode remains constant since the lattice volume did not shrink or expand due to the fact that amount of the Ag and Ge content in the lattice structure are low and close to each other. The Raman peak intensities of the sample produced with 1°C /s are relatively higher by twofold indicates the improved crystal quality. Overall, according to the Raman measurements, the optimum heating rate for the growth of Ag and Ge co-doped CZTS thin film was determined as 1°C/s.

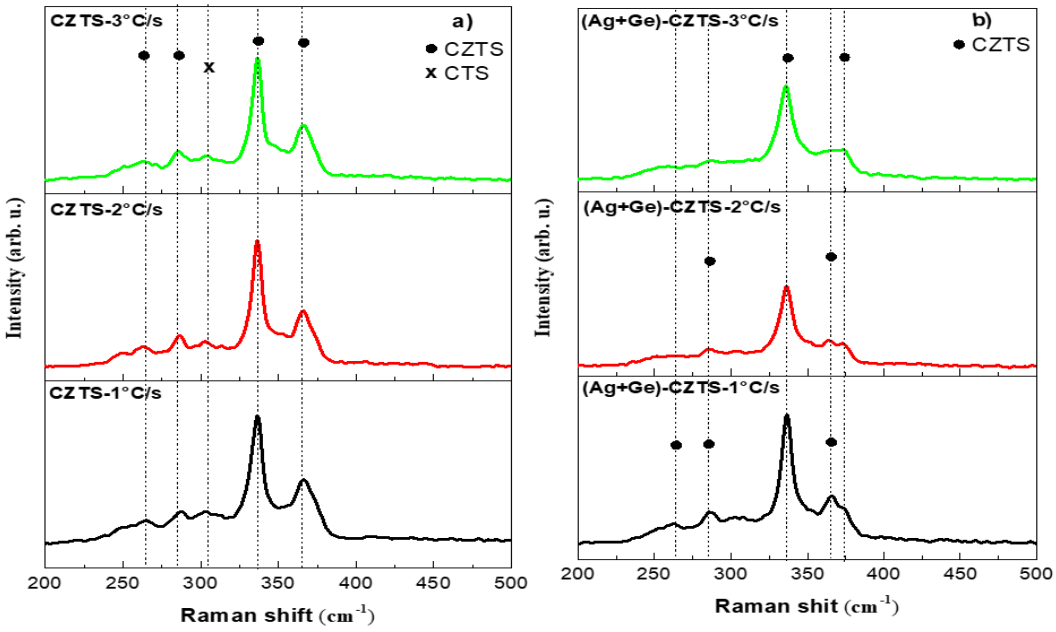

Figure 3. Raman spectra of a) undoped, b) Ag+Ge co-doped CZTS thin films formed employing various heating rates.

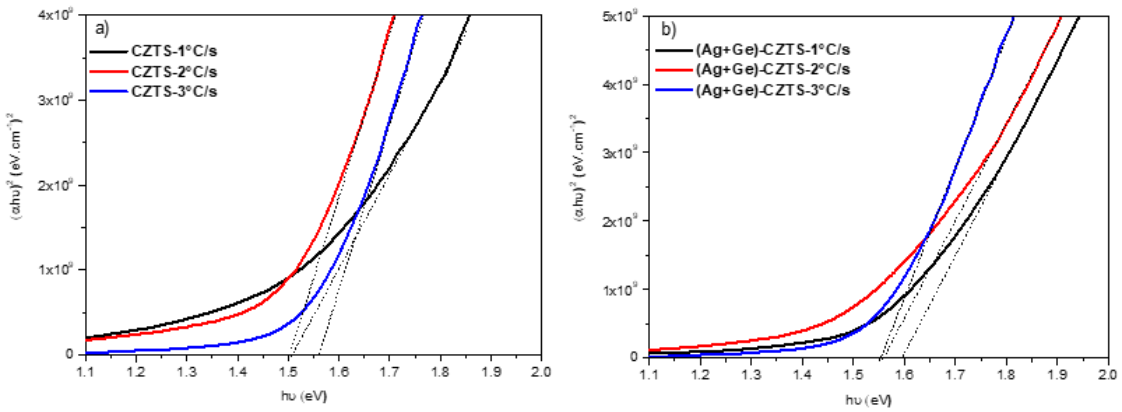

Figure 4. Determination band gap of a) undoped, b) Ag+Ge co-doped CZTS thin films from $(\alpha h\nu)^2$ - $(h\nu)$ curves.

The transmission data were taken in the wavelength range of 400-1200 nm of the CZTS samples grown by employing various heating rates. The optical direct bandgap of the samples was determined using Tauc plot equation of $(\alpha h\nu) = A(h\nu - Eg)^{1/2}$ with known absorption coefficients calculated from transmission data [24]. Then, the direct bandgap values of the undoped and Ag+Ge co-doped samples were obtained from the points where the linear region of the curve intersect on the $h\nu$ - axis. While the band gap value of undoped CZTS thin films produced at 1°C/s and 2°C/s was found to be 1.5 eV, this value increased up to 1.56 eV with the heating rate of 3°C/s [25]. In contrast, the bandgap values of the Ag and Ge co-doped CZTS thin film produced at higher heating rates (2-3°C/s) did not show a substantial change. On the other hand, it was determined that the bandgap energy increased to 1.6 eV with an increase of 0.1 eV compared to undoped CZTS with the sample produced by 1°C/s. This may be due to the fact that the doping atoms cannot sufficiently introduce into the lattice structure for the samples produced at higher heating rates. Optical measurements show that the annealing time of 1 minute is sufficient to obtain the desired structure for the Ag and Ge co-doped sample sulfurized at 550°C with the heating rate of 1°C/s.

4. CONCLUSION

The effect of heating rate on the structural and optical properties of Ag+Ge co-doped CZTS thin film were studied and compared with undoped CZTS structure. The precursor stacks formed by the sequential deposition of Cu, Sn, ZnS, Ag and Ge layers via sputtering system, then were sulfurized at 550°C for 1 minute in the RTP system employing various heating rates. The EDS measurements indicated that Ag and Ge co-doped precursor stack have a Cu-poor, Zn-rich chemical composition with a close targeted dopant content. Although the kesterite CZTS structure took place in all of the samples according to XRD patterns and Raman spectra, secondary phase formation and crystal quality changed with the employing different heating rate. Overall, Ag and Ge co-doped CZTS sample produced with a heating rate of 1°C/s revealed better results due to formation single phase and successfully incorporation of Ag and Ge ions into the kesterite structure. In our future works, we will focus on investigating the effect of different ratios of cation replacement on the properties of CZTS thin film as well as device performance.

SIMILARITY RATE: 13%

ACKNOWLEDGEMENT

This work was supported by grants from Scientific Research Projects Unit of Niğde Ömer Halisdemir University (FMT 2022/6-BAGEP). The authors also thanks to Prof. Dr. RECEP ZAN for his valuable support.

REFERENCES

[1] K. Jimbo *et al.*, "Cu2ZnSnS4-type thin film solar cells using abundant materials," *Thin solid films,* vol. 515, no. 15, pp. 5997-5999, 2007.
[2] K. Ito, *Copper zinc tin sulfide-based thin-film solar cells*. John Wiley & Sons, 2014.
[3] M. A. Green *et al.*, "Solar cell efficiency tables (Version 61)," *Progress in Photovoltaics: Research and Applications,* 2023.
[4] W. Shockley and H. J. Queisser, "Detailed Balance Limit of Efficiency of p-n Junction Solar Cells," (in English), *J. Appl. Phys.,* vol. 32, no. 3, pp. 510-519, 1961, doi: 10.1063/1.1736034.
[5] Y. E. Romanyuk *et al.*, "Doping and alloying of kesterites," *Journal of Physics: Energy,* vol. 1, no. 4, p. 044004, 2019.
[6] S. G. Haass, M. Diethelm, M. Werner, B. Bissig, Y. E. Romanyuk, and A. N. Tiwari, "11.2% efficient solution processed kesterite solar cell with a low voltage deficit," *Advanced Energy Materials,* vol. 5, no. 18, p. 1500712, 2015.
[7] S. Giraldo *et al.*, "Cu2ZnSnSe4 solar cells with 10.6% efficiency through innovative absorber engineering with Ge superficial nanolayer," *Progress in Photovoltaics: Research and Applications,* vol. 24, no. 10, pp. 1359-1367, 2016.
[8] S. Yang *et al.*, "The impact of different Ag/(Ag+ Cu) ratios on the properties of (Cu 1− x Ag x) 2 ZnSnS 4 thin films," *Journal of Materials Science: Materials in Electronics,* vol. 30, pp. 11171-11180, 2019.
[9] Y. Atasoy, "Effect of annealing temperature on the microstructural and optical properties of newly developed (Ag, Cu) 2Zn (Sn, Ge) Se4 thin films," *Applied Physics A,* vol. 128, no. 11, p. 1030, 2022.
[10] L. Qiu, J. Xu, and X. Tian, "Fabrication of Ag and Mn co-doped Cu2ZnSnS4 thin film," *Nanomaterials,* vol. 9, no. 11, p. 1520, 2019.

[11] X. Zhao *et al.*, "Lithium-assisted synergistic engineering of charge transport both in GBs and GI for Ag-substituted Cu2ZnSn (S, Se) 4 solar cells," *Journal of Energy Chemistry*, vol. 50, pp. 9-15, 2020.
[12] A. Yagmyrov, S. Erkan, B. Başol, R. Zan, and M. Olgar, "Impact of the ZnS layer position in a stacked precursor film on the properties of CZTS films grown on flexible molybdenum substrates," *Optical Materials*, vol. 136, p. 113423, 2023.
[13] A. Fairbrother *et al.*, "Precursor stack ordering effects in Cu2ZnSnSe4 thin films prepared by rapid thermal processing," *The Journal of Physical Chemistry C*, vol. 118, no. 31, pp. 17291-17298, 2014.
[14] M. Olgar, A. Sarp, A. Seyhan, and R. Zan, "Impact of stacking order and annealing temperature on properties of CZTS thin films and solar cell performance," *Renewable Energy*, vol. 179, pp. 1865-1874, 2021.
[15] S. Y. Chen, X. G. Gong, A. Walsh, and S. H. Wei, "Defect physics of the kesterite thin-film solar cell absorber Cu2ZnSnS4," (in English), *Appl Phys Lett*, vol. 96, no. 2, p. 021902, Jan 11 2010, doi: Artn 02190210.1063/1.3275796.
[16] A. R. Denton and N. W. Ashcroft, "Vegard's law," *Phys. Rev. A*, vol. 43, no. 6, p. 3161, 1991.
[17] N. Saini, J. K. Larsen, K. V. Sopiha, J. Keller, N. Ross, and C. Platzer-Björkman, "Germanium incorporation in Cu2ZnSnS4 and formation of a Sn–Ge gradient," *physica status solidi (a)*, vol. 216, no. 22, p. 1900492, 2019.
[18] H. Cui, X. Liu, F. Liu, X. Hao, N. Song, and C. Yan, "Boosting Cu2ZnSnS4 solar cells efficiency by a thin Ag intermediate layer between absorber and back contact," *Appl Phys Lett*, vol. 104, no. 4, p. 041115, 2014.
[19] M. Y. Valakh *et al.*, "Raman scattering and disorder effect in Cu_2ZnSnS_4," *physica status solidi (RRL)–Rapid Research Letters*, vol. 7, no. 4, pp. 258-261, 2013.
[20] S. Yazici *et al.*, "Growth of Cu_2ZnSnS_4 absorber layer on flexible metallic substrates for thin film solar cell applications," (in English), *Thin Solid Films*, vol. 589, pp. 563-573, Aug 31 2015, doi: 10.1016/j.tsf.2015.06.028.
[21] M. Olgar, A. Seyhan, A. Sarp, and R. Zan, "The choice of Zn or ZnS layer in the stacked precursors for preparation of Cu2ZnSnS4 (CZTS) thin films," *Superlattices and Microstructures*, vol. 146, p. 106669, 2020.
[22] J. J. Scragg, L. Choubrac, A. Lafond, T. Ericson, and C. Platzer-Björkman, "A low-temperature order-disorder transition in Cu2ZnSnS4 thin films," *Applied Physics Letters*, vol. 104, no. 4, p. 041911, 2014.
[23] H. D. Shelke, A. C. Lokhande, V. S. Raut, A. M. Patil, J. H. Kim, and C. D. Lokhande, "Facile synthesis of Cu 2 SnS 3 thin films grown by SILAR method: effect of film thickness," *Journal of Materials Science: Materials in Electronics*, vol. 28, pp. 7912-7921, 2017.
[24] J. Tauc, "Optical properties and electronic structure of amorphous Ge and Si," *Mater. Res. Bull.*, vol. 3, no. 1, pp. 37-46, 1968.
[25] B. A. Schubert *et al.*, "Cu2ZnSnS4 thin film solar cells by fast coevaporation," *Progress in Photovoltaics: Research and Applications*, vol. 19, no. 1, pp. 93-96, 2011.

Eurasian Journal of Science Engineering and Technology

Research Article

TREATMENT OF TEXTILE WASTEWATER WITH CHERRY LAUREL LEAVES AND WASTE POTATO PEELS

Şennur Merve YAKUT[1,*]

[1] *Nevsehir Haci Bektas Veli University, Faculty of Engineering and Architecture, Department of Environmental Engineering, 50300, Nevşehir, Türkiye*

ABSTRACT

In this study, a research was carried out on the removal of dyestuff, which is a big problem in the textile industry. The adsorption method was used for the removal of Maxilon Yellow 4GL dyestuff. Cherry laurel leaf (*Prunus laurocerasus*) and waste potato peels were used as adsorbent, and the removal efficiency was determined as 76.64% at pH 7 and with 2 g adsorbent, 80% dyestuff removal efficiency was achieved in the specified conditions for cherry laurel leaves. For experiments in which waste potato peels were used as adsorbent, the optimum conditions were found as follows: Contact time: 60 minutes, adsorbent concentration of 0.75 grams and initial concentration of 25 mg/L. The Freundlich isotherm model was suitable for our study, since the regression number was found to be 0.999 for cherry laurel leaves and 0.995 for waste potato peels as a result of isotherm studies. According to the cost analysis, the materials supplied free of charge, due to mixing, the electricity cost for treatment (0.128 TL) and the chemical material cost is 17 TL, and it has been determined that these adsorbents are quite economical in dyestuff treatment. As a result, the fact that there is no study on the removal of cherry laurel leaves with the mentioned dyestuff in the literature shows that this study can be further developed.

Keywords: Adsorption, Dye removal, Cherry Laurel leaf, Waste potato peels.

1. INTRODUCTION

Increasing environmental concerns have led scientists to use natural materials for the environment. The rise in population has increased the demand for textile products. Therefore, more production caused more water pollution. The main environmental problem for the textile industry is colored wastewater. Since dyestuffs have toxic properties and have a carcinogenic effect on metabolism, they must be purified from wastewater. In addition, when these waters are mixed with the discharge environment, the dyestuffs in it reduce the photosynthesis by blocking the sun rays. The presence of these substances in the aquatic environment causes great damage to the aquatic ecosystem [1]. Most of the dyes are organic and consist of chromogen and auxochrome groups. Of these, auxochrome groups provide binding to textile products. When these groups are bonded with molecules, a shift can occur in the visible region and these groups are called "chromophore groups" or "color forming groups". The main ones are as follows: [2]:

Nitroso group: -NO or =N-OH
Nitro group : $-NO_2$
Azo group : -N=N
Ethylene group : -C=C
Carbonyl group : -C=O

One of the most commonly used methods for dye removal from textile wastewater is adsorption. When an atom, ion or molecule is brought into contact with a solid, some of the atoms, ions or molecules are held by the solid. If this holding process takes place on the surface of the solid, it is called adsorption. The substance adsorbed to the substance whose concentration increases on the liquid or solid surface is called adsorbate, and the substance that adsorbs is called adsorbent [3].

Usage areas of the adsorption process:

- Dechlorination
- Removal of persistent organic pollutants found in industrial waste
- Dye removal
- Reducing the need for chlorine
- Removal of undesirable odor and taste
- Removal of toxic compounds [4].

In this study, powders of cherry laurel leaves and waste potato peels were used as adsorbent material. The cherry laurel plant, which is grown in the Black Sea region of Turkey, has an antioxidant effect due to its phenolic contents. It is found in many

* Corresponding author, e-mail: sennurmerve@nevsehir.edu.tr (Ş. M. Yakut)
Recieved: 14.05.2023 Accepted: 07.06.2023
doi: 10.55696/ejset.1296953

countries in the world, especially in Europe and Iran, and it is frequently used as an ornamental plant [5]. Potato is an antioxidant like other adsorbent and is widely consumed [6].Therefore, it creates a large amount of domestic waste potential. It will be very useful to use the waste potato peels, which are turned into adsorbent by a simple process, in the removal of the color parameter in the textile industry wastewater.

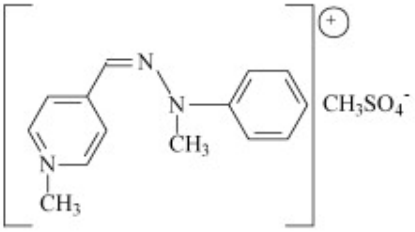

Figure 1. Maxilon yellow 4GL [7]

Maxilon yellow 4GL (Figure 1) which is used in experimental a cationic dye. Since their colored parts are in the form of cations, these dyes are defined as cationic dyestuffs. Cationic dyes are currently used in large quantities for dyeing acrylics and modified acrylics [8]. The reason for choosing this dye in the study is that it is a reactive dye. The difference of reactive dyes from other dyes is that they can react with large molecules in the fibers and form real bonds. [2,9].The characteristics of the dye are shown in Table 1 [10,11].

Table 1. The characteristics of dye

Name	Color	Color Index	Molecular Weight	Molecular formula
Maxilon Yellow 4GL	Basic Yellow	87	337.39	$C_{15}H_{19}N_3O_4S$

The aim of this study is to investigate the use of some materials found in nature in wastewater removal. Harmful chemicals are used in the removal of color parameter from the colored wastewater of the textile industry, which is one of the main environmental problems, and new materials are used as alternatives to these harmful chemicals. For this purpose, cherry laurel tree leaves and potato peels were used in the study.

2. MATERIAL AND METHOD

Cherry laurel leaves were freshly collected from Düzce, Turkey. Afterwards, it was thoroughly washed with tap water in order to avoid any residue (dust, insects, etc.) on it. Then the leaves were washed with deionized water and dried in a sunny room for 1 week. Throughly dried leaves were passed through a kitchen grinder and stored in an airtight container. In this way, it is ready for the experimental stage. The chemical materials used in the study were of analytical purity and ultrapure water was used at every stage to prevent any unwanted interference. The same procedure was followed for waste potato peels. Digital scale (Radwag), shaker incubator (JSR), pomp (Rocker), spectrophotometer (Hach lange dr3900) and pH meter (Hach lange hd30d) were used in the analysis phase.

Before starting the experiments, the target pollutant prepared at certain concentrations was measured in the spectrophotometer in order to understand the results. In this context, certain amounts of dilution were made from the stock solution prepared as 100 mg/L then, solutions were prepared at concentrations of 5 mg/L, 10 mg/L, 15 mg/L and 25 mg/L, and adsorbance readings were made in the device at 410 nm.

After the solutions prepared at the concentrations stated in the second section were read in the spectrophotometer, a calibration graphic was drawn. In this context, experiments were carried out. In the next experiments, the adsorbent values read in the spectrophotometer were converted to concentration using this equation.

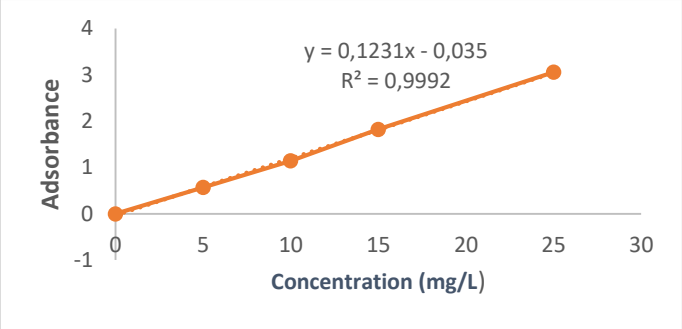

Figure 2. Calibration graphic

The relevant graphic is shown on the Figure 2. The correlation coefficient was found to be 0.999. The linearity of the graph indicated that good calibration solutions were prepared.

2.2. Adsorption Studies

In order to investigate the effect of pH on dyestuff removal, the initial dyestuff solution was using 0.1 N NaOH and 0.1 N HCl solutions at pH of 3, 5, 7, 9 and 11 set at room temperature. In order to examine the effect of temperature on dye removal, samples were taken at 25, 35 and 45 degrees. The effect of initial concentration was determined by experimenting with concentrations between 5-25 mg/L. In order to determine the contact time of the cherry laurel leaves and waste potato peels in the removal of the dyestuff, samples were taken and measured at certain times different minutes. In order to determine the effect of the amount of the adsorbents on the removal of the dye, 0,1-2 grams of leaves were added.

2.2. Isoterm and Kinetic Studies

The kinetic study was carried out considering the optimum conditions where the highest dyestuff removal was achieved. In this context, Freundlich isotherm model, which is one of the most frequently used isoterm models in adsorption studies, was used. The formula for the relevant model is shown in Equation (1) and Equation (2). Here, the correlation coefficient (R^2) must be taken into account. The closer this number is to 1, the closer it is to linearity [12].

$$q = \frac{x}{m} = Kf.Ce^{(\frac{1}{n})} \quad (1)$$

The equation is expressed logarithmically as:

$$\log\left(\frac{x}{m}\right) = logKf + \left(\frac{1}{n}\right) logCe \quad (2)$$

Ce (mg/L) is the equilibrium concentration, q (mg/g) is the adsorption amount at equilibrium, x (mg/L) is the concentration of adsorbed solute, K_f is adsorption capacity, n is adsorption intensity [12].

As the kinetic model, 1st order, 2nd order and additionally the kinetic model they studied in Behnajady et al. (2007) was used [13,14].

1. order kinetic model: $Ct = Co\, e^{-k1\, t}$ (3)
2. order kinetic model: $\frac{1}{Ct} = \frac{1}{Co} + k_2 t$ (4)

In the equations given in Equations 3 and 4, C is the concentration of maxilon yellow 4gl and t is the time. k_1 and k_2 are 1st and 2nd order kinetic constants, respectively. Co is the starting concentration of maxilon yellow 4 GL.

The kinetic model formula used by Behnajady et al. in their study is shown in Equation 5. Here, the b represents the degradation value of the pollutants.

$$\frac{Ct}{Co} = 1 - \frac{1}{b} \quad (5)$$

3. RESULTS AND DISCUSSION

3.2. pH Effect

As it is known, pH is an important parameter in adsorption. For this purpose, adjustments were made at different pH values. First of all, initial concentration (Co) was adjusted 25 mg/L, amount of adsorbent (A_a) was 1 g/L and contact time was 60 minutes. According to the data obtained from the adsorption studies performed at acidic, neutral and basic values, the highest dyestuff removal was obtained in neutral conditions. As seen in Figure 3, the best dye removal efficiency was achieved at pH 7.

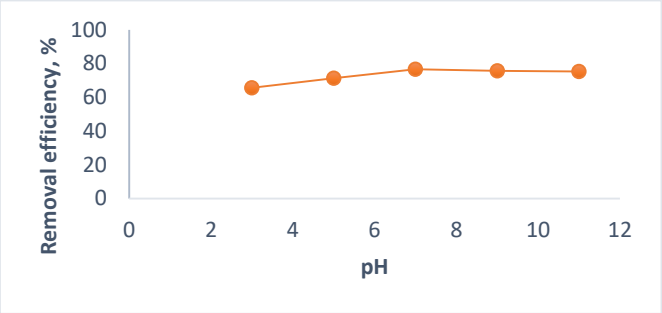

Figure 3. pH effect (Co:25 mg/L, A_a : 1 g/L, Time: 60 min.)

The reason why the removal efficiency is higher at high pH values is that the adsorbent is more effective in removing cations because OH- ions are coated on the surface of the adsorbent at high pH [15]. In addition, with the increase in pH, the adsorbent surface is negatively charged and attracts Maxilon Yellow 4GL, a cationic dye. Therefore, it is thought that dye removal is higher at neutral and basic pH values. [16].

3.3. Temperature Effect

According to the results obtained, the dye removal of the adsorbent little decreased as the temperature increased. As the reason for this, it can be concluded that the efficiency decreased because of the deterioration of the temperature on the adsorbent. Figure 4 shows that, high temperature is not suitable for this adsorbent. However, the effect of temperature is negligible as the reduction is very small.

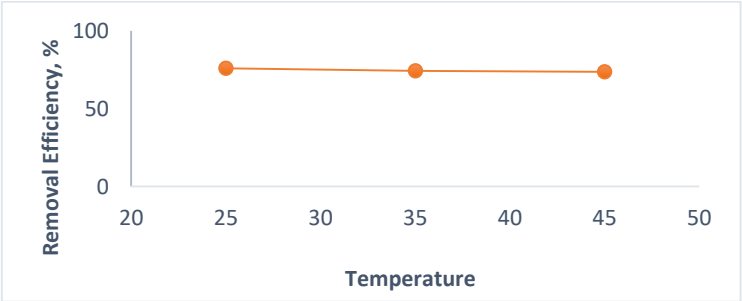

Figure 4. Temperature effect (pH: 7, C_o:25 mg/L, A_a: 1 g/L, Time: 60 min.)

pH and temperature values was studied for cherry laurel leaves. These parameters were not studied in other adsorbent to see how much efficiency can be obtained without using much chemicals and spending energy for extra heating.

3.4. Contact Time Effect

As seen in the Figure 5, for cherry laurel leaves, adsorption increased with increasing contact time. However, after the 90th minute, the reaction reached equilibrium, that is, there was no significant increase. It can be said that the reason for this is that the pores of the leaves are filled with adsorption in the first stage, and then these pores cannot achieve more dyestuff retention.

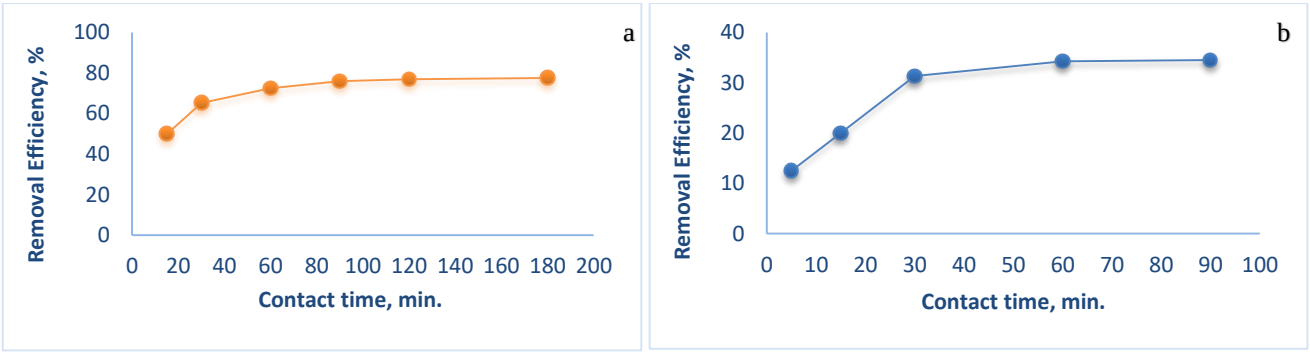

Figure 5. Contact time effect, cherry laurel leaf (a), waste potato peel (b)

For the studies in which waste potato peels were used as adsorbent, pH 7, initial dyestuff concentration of 25 mg/L and temperature were adjusted as room temperature. As seen in Figure 5 (b), an increase in removal efficiency is observed until the 60th minute, then the solution reaches equilibrium. At first, a rapid adsorption was observed because the pores on the surface of the adsorbent were open, while a slowdown in adsorption was observed as the pores filled over time [16]. Therefore, cherry laurel leaves reached equilibrium at 90 minutes and waste potato peels reached equilibrium at 60 minutes. However, the dye removal efficiency was lower than the other adsorbent (waste potato peels).

3.5. Adsorbent Concentration

According to the results obtained for cherry laurel leaves, 40.8% color removal was observed when 0.1 grams of adsorbent was added, 62.6% when 0.5 grams was added, 76% when 1 gram was added, and 80% when 2 grams were added, 78.76 when 2.5 grams were added. With the addition of adsorbent up to a certain amount, the removal efficiency increases and it is fixed after a point, indicating that the adsorbent has reached saturation for cherry laurel leaves.

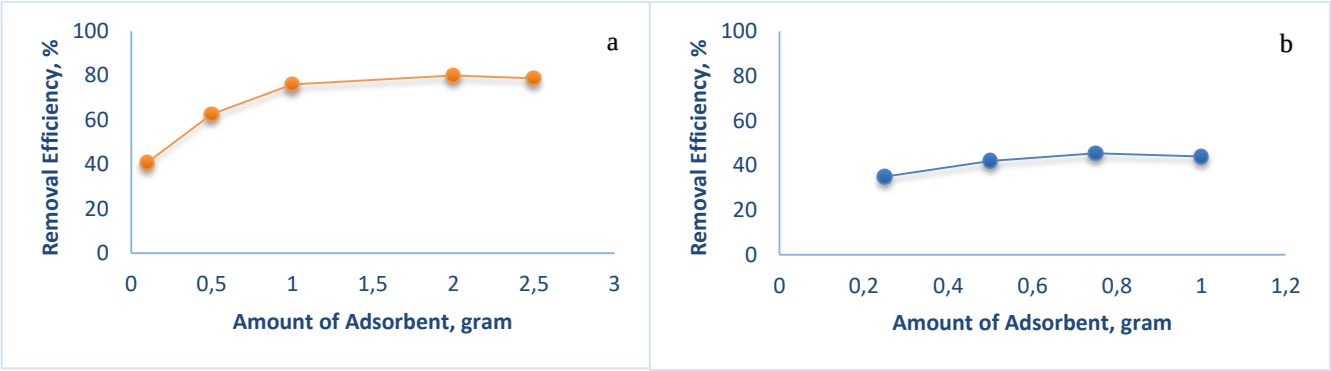

Figure 6. Amount of adsorbent effect

As seen in Figure 6 (b), the adsorbent added as 0.25, 0.5 0.75 and 1g/L reached the most efficient value at 0.75 g/L. Since the small amount of adsorbent could not adsorb the dyestuff, the dyestuff removal efficiency increased as the amount of adsorbent increased. However, there was a slight decrease in the dye removal efficiency afterwards. The reason for this suggests that the waste potato peels may give a yellowish color in the solution due to its structure.

3.6. Initial Concentration

Components in low concentration dyestuffs have difficulty interacting with each other. Thus, the adsorption rate of the dye increases. In the case of an increase in dye concentration, the dye removal efficiency decreases as the mentioned components compete with each other [17].

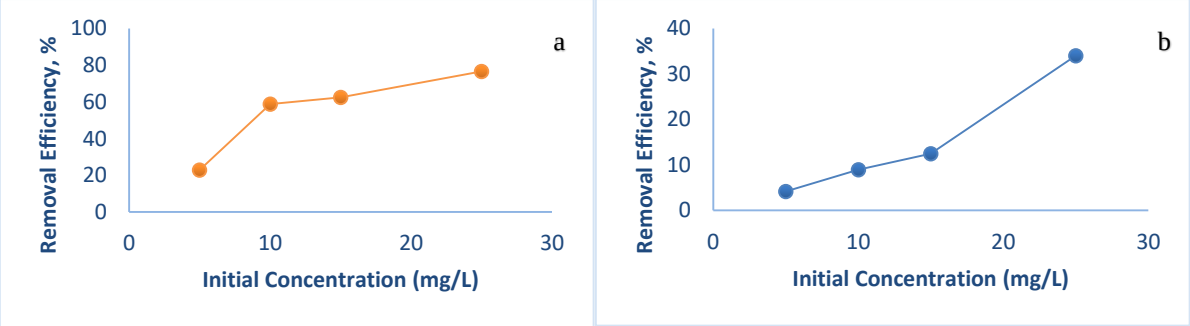

Figure 7. Initial concentration effect

Figure 7 shows a leap in dye removal after an initial concentration of 15 mg/L for both adsorbents. Therefore, for both adsorbents, the dye removal efficiency increased as the dye concentration increased.

3.7. Isoterm and Kinetic Studies

Freundlich isotherm model, which is one of the most used isotherms, has been applied to understand the balance between Maxilon Yellow 4GL dye, which is a residue in aqueous solution, and Maxilon Yellow 4GL dye adsorbed. Figure 8 (a is for cherry laurel leaves and b is for waste potato peels), shows that, a high correlation coefficient was obtained for the Freundlich isotherm. This means that the adsorbent heterogeneous adsorption has taken place and it shows that the adsorption is successful [18]. Also, Langmuir isotherm studies carried out. Although the high correlation coefficient was high for the Langmuir isotherm for cherry laurel leaves, a lower correlation coefficient was found for the Langmuir isotherm for waste potato peels.

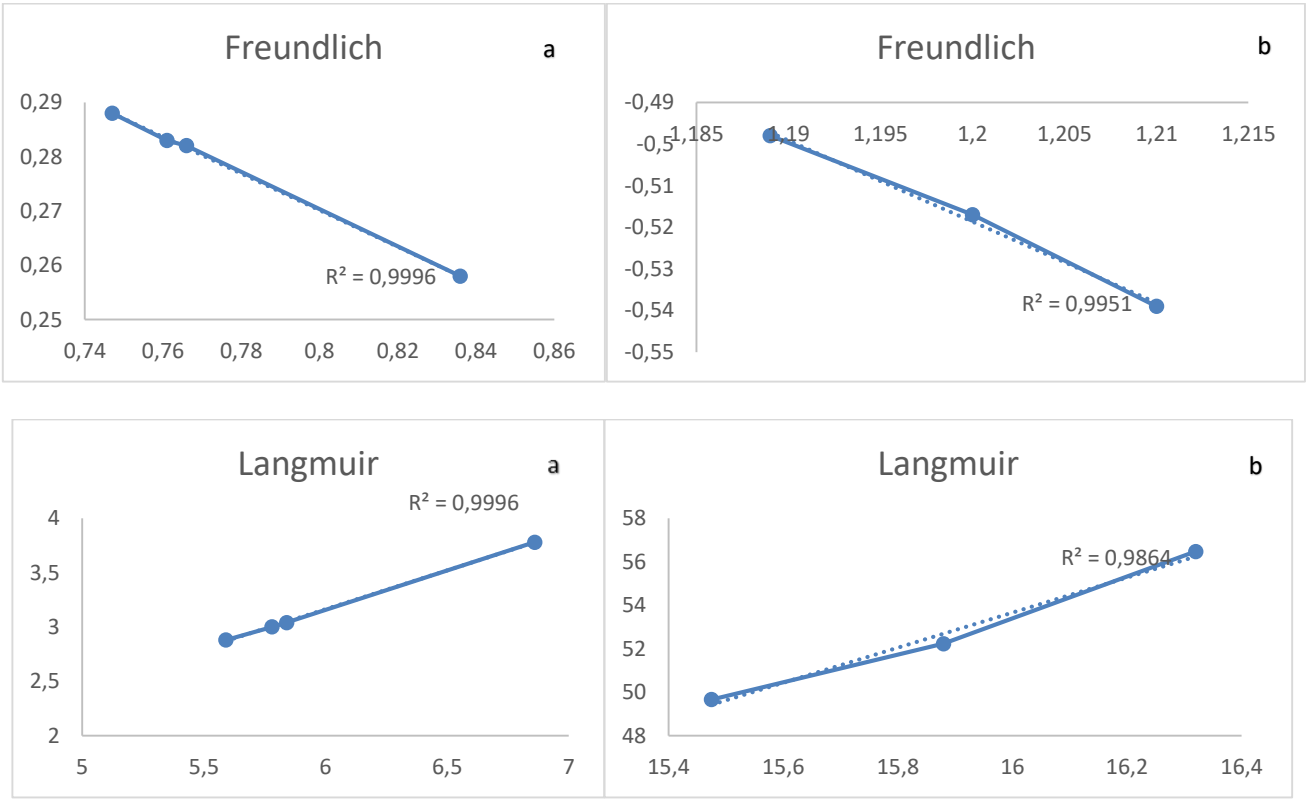

Figure 8. Isotherm graphics

Table 2. Correlation coefficients according to the kinetic model

Adsorbent	First order kinetic	Second order kinetic	Behnajady kinetic model
Cherry Laurel Leaves	0.778	0.776	0.999
Waste Potato Peels	0.984	0.999	0.999

Table 2 shows the kinetic studies. The results show that the Behnajady kinetic model is suitable for both adsorbents.

As can be seen in Table 3, studies in the literature have generally worked with high amounts of adsorbent. The advantage of this study compared to similar studies is that it works at lower adsorbent doses. In addition, dyestuff removal is observed in a short time in this study.

Table 3. Similar studies in the literature

Dyestuff	Adsorbent	Removal Efficiency	Amount of Adsorbent	References
Methylene blue	Rice Straw	91%	1 g/L	[19]
Direct Yellow	Zeolite, wood ash, wood shavings	37%	10 g/L	[20]
Verfix red and Lanasyam brown GRL	Carbon and flyash	100%	10 g/L	[21]
Rodamin B and Malachite Green	Biochar	99.05% and 98.08%	0.1 g/mL	[22]
Malachite green and Methylene blue	Annona skumosa seed	75.66% and 24.33%	0.2 g/50 mL	[23]
C.I.Acid Violet 90 and C.I.Acid Yellow 194	Egg shell	82.3 % and 91.5%	3-25 g/L	[24]

3.8. Cost Analysis

The use of low-cost alternative adsorbents is very important for the environment. Today, the use of adsorbents produced by expensive methods creates an extra burden for the environment and restricts treatment due to some toxic chemicals used in production. The fact that one of the adsorbents selected in this study is a plant grown in nature and the other is a waste food product makes the adsorbent material free. If we take into account only the electricity consumed by the shaker for treatment, the electricity cost is approximately 1,425 TL/kWh *0.09 KWh = 0,12825 TL (excluding taxes) in an hour for May/2023. Since tap water is only used to wash organic materials, there is a consumption of approximately 10 liters. Since 0.2 mL of HCl solution was used per solution to adjust the pH, approximately 25 mL was used in total. According to the current exchange rate, 1 liter of HCl is approximately 665 TL. Therefore, the acid consumption is 17 TL. Thus, it is possible to use Maxilon Yellow 4GL for the removal of dyestuff at a very low cost.

4. CONCLUSION

Maxilon Yellow 4GL removal was done by using leaves of cherry laurel leaves and waste potato peels, and no study was found in the literature in which this dyestuff was removed with the mentioned adsorbents. As a result of a series of experimental studies, the optimum conditions for dye removal were determined as follows: pH, 7; the temperature is 25 degrees; the contact time was 90 minutes and the amount of adsorbent was 1 gram for cherry laurel leaves. The optimum conditions for dye removal were determined as follows: the contact time was 60 minutes, initial concentration was 25 mg/L and the amount of adsorbent was 0.75 gram for waste potato peels. According to the data we obtained, the removal of Maxilon Yellow 4GL, a textile dye, was accomplished with cherry laurel leaves without applying any additional chemical treatment. The highest efficiency was obtained as 80%. In addition, the fact that it is a natural removal is the strongest advantage of this method. For waste potato

peels, the highest efficiency was 45 %. Although the dye removal efficiency of waste potato peels is lower than other adsorbent, it is thought that the removal efficiency will increase by applying different modifications on it. Here, the adsorbents, which are divided into small pieces, interact with the pollutant and adhere to the surface of the adsorbent. Potato peels appear to have a low effect on the color removal mechanism due to the yellow coloration of the aqueous medium. As a result, under optimum conditions, 76.6% for cherry laurel leaves; 34% removal efficiency was obtained for waste potato peels. There are many pollutants in the content of textile industry wastewater and the main of these pollutants are dyestuffs. These pollutants create a large amount of Chemical Oxygen Demand, especially during dyeing processes, there is a lot of water consumption. For these reasons, the color parameter, which is only one of the parameters that creates the pollution load, was chosen in this study. It is thought that these materials will be studied on the removal of other pollutant parameters in future studies.

SIMILARITY RATE: 10%

CONFLICT of INTEREST

The authors declared that they have no known conflict of interest.

ACKNOWLEDGEMENT

I thank the organization and the scientific committee for the opportunity to present this work at the 5th International Conference on Materials Science, Mechanical and Automotive Engineerings and Technology (IMSMATEC'22) held in September, 2022.

REFERENCES

[1] K. M. Ayvaz & M. S. Teker, "Türkiye'de doğal boya kullanan tekstil işletmeleri ve bitki atıkları ile sürdürülebilir bir yaklaşım önerisi", *Yüzüncü Yıl Üniversitesi Sosyal Bilimler Enstitüsü Dergisi*, vol. 59, pp. 348-362, 2023.

[2] C. Yıldız, "Maxilon yellow 4gl boyar maddesinin bazı oksit mineralleri yüzeyine adsorpsiyonuna ait deneysel dizaynı ve optimizasyonu", *Balıkesir Üniversitesi, Fen Bilimleri Enstitüsü, Yüksek Lisans Tezi,* 2013.

[3] H. Abak, "Sulu çözeltilerden metilen mavisinin fındık kabuğu yüzeyine adsorpsiyon ve adsorpsiyon kinetiği", *Balıkesir Üniversitesi, Fen Bilimleri Enstitüsü, Yüksek Lisans Tezi*, 2008.

[4] K. Kestioğlu, *Çevre Mühendisliğinde Fiziksel ve Kimyasal Temel İşlemler*. Bursa: Uluçev, 2011.

[5] A. İslam & H. Deligöz, "Ordu ilinde karayemiş (Laurocerasus officinalis L.) seleksiyonu", *Akademik Ziraat Dergisi*, vol.1, no. 1, pp. 37-44, 2012.

[6] S.A. El-Sawi, M. E. Ibrahim, R.I. Bassuiny & R. M. Merghany, "Antioxidant, cytotoxic and antimicrobial efficacy of potato peels, taro peels, and husk and silk of corn", *Proceedings of the National Academy of Sciences, India Section B: Biological Sciences*, pp. 1-8, 2023.

[7] M. Doğan, M. H: Karaoğlu & M. Alkan," Adsorption kinetics of maxilon yellow 4GL and maxilon red GRL dyes on kaolinite", *Journal of Hazardous Materials*, vol. 165, no. 1-3, pp. 1142-1151, 2009.

[8] O. Al, "Tekstil atıksularındaki katyonik boyar maddelerin fizikokimyasal arıtımı", *İstanbul Üniversitesi-Cerrahpaşa, Lisansüstü Eğitim Enstitüsü, Yüksek Lisans Tezi*, 2019.

[9] Tekay Kimya, "*Reaktif Boyalar"*2023. [Online]. Available: https://www.tekaykimya.com.tr/home/reaktif-boyalar/. [Accessed: May. 28, 2023].

[10] Guidechem," *Maxilon Yellow M 4GL"* 2023. [Online]. Available: https://www.guidechem.com/dictionary_keys_Maxilon+Yellow+M+4GL-p1.html. [Accessed: May. 28, 2023].

[11] Classic Dyestuffs, Inc.Product Catalog, *"Basic"* 2023. [Online]. Available: https://classicdye.com/pdf/catalog.pdf. [Accessed: May. 28, 2023].

[12] A. Proctor & J. F. Toro-Vazquez, "The Freundlich isotherm in studying adsorption in oil processing", *Journal of the American Oil Chemists' Society,* vol. 72, pp. 1627-1633, 1996.

[13] S. Şahinkaya, "COD and color removal from synthetic textile wastewater by ultrasound assisted electro-Fenton oxidation process", *Journal of Industrial and Engineering Chemistry*, vol. 19, pp. 2, 601-605, 2013.

[14] M. A. Behnajady, N. Modirshahla & F. Ghanbary, "A kinetic model for the decolorization of CI Acid Yellow 23 by Fenton process", *Journal of Hazardous Materials*, vol. 148, no.(1-2), pp. 98-102, 2007.

[15] Ü. A. Güler, "Aljinat-TiO2-alg kompozitinin sentezi ve sulu çözeltilerden tetrasiklin gideriminde kullanılabilirliği ve karakterizasyonu", *Karaelmas Fen ve Mühendislik Dergisi,* vol. 6, no. 1, pp. 130-135, 2016.
[16] A. Yıldız, "Aktive edilmiş ceviz kabuğuna boyar madde adsorpsiyonu", *Bozok Üniversitesi, Fen Bilimleri Enstitüsü, Yüksek Lisans Tezi,* 2014.
[17] B. Demir & Y. Kalpaklı, "İşlem görmemiş Kütahya Ca-bentonitinin bazik mavi 41 (BB41) adsorpsiyon karakteristiğinin incelenmesi", *Journal of the Institute of Science and Technology,* vol. 10, no.1, pp. 309-319, 2020.
[18] F. C. Çavuşoğlu, Ş. S. Bayazit & M. A. Salam, "Montmorillonit bazlı nanokiller kullanılarak kristal viyolet boyar maddesinin sulu çözeltilerden giderimi: Kinetik ve denge çalışmaları", *Gazi Üniversitesi Mühendislik Mimarlık Fakültesi Dergisi,* vol. 38, no.3, pp. 1907-1918, 2023.
[19] G. Kaykıoğlu & İ. S. Dalmış," Piroliz uygulanmış çeltik sapları ile sulu çözeltilerden renk giderimi". *Doğal Afetler ve Çevre Dergisi*, vol. 6, no. 1, pp. 37-48, 2020.
[20] İ. K. Kapdan & F. Kargı, "Atıksulardan tekstil boyar maddelerinin adsorpsiyonlu biyolojik arıtım ile giderimi". *Turkish Journal of Engineering and Environmental Sciences*, vol.24, pp.161-169, 2000.
[21] K. Ravikumar, S. Ramalingam, S. Krishnan & K. Balu, "Application of response surface methodology to optimize the process variables for reactive red and acid brown dye removal using a novel adsorbent". *Dyes and pigments,* vol. 70, no.1, pp.18-26, 2006.
[22] S. Cheng, S. Zhao, B. Xing, Y. Liu, C. Zhang & H. Xia, "Preparation of magnetic adsorbent-photocatalyst composites for dye removal by synergistic effect of adsorption and photocatalysis". *Journal of Cleaner Production*, vol. 348, no.131301, 2022.
[23] T. Santhi, S. Manonmani, V. S. Vasantha & Y. T. Chang. "A new alternative adsorbent for the removal of cationic dyes from aqueous solution". *Arabian Journal of Chemistry*, vol.9, pp. 466-474, 2016.
[24] M. Okur, "Tekstil atıksularındaki metal kompleks boyarmaddelerin yumurta kabukları ile giderimi". *Gazi Üniversitesi Mühendislik Mimarlık Fakültesi Dergisi*, vol.28, no.4, pp. 777-785, 2013.

Eurasian Journal of Science Engineering and Technology

Research Article

INVESTIGATION OF STRUCTURAL, OPTICAL, AND ELECTRICAL PROPERTIES OF ITO FILMS DEPOSITED AT DIFFERENT PLASMA POWERS: ENHANCED PERFORMANCE AND EFFICIENCY IN SHJ SOLAR CELLS

Emre KARTAL [1 *], İlker DURAN [2], Elif DAMGACI [3] Ayşe SEYHAN [4]

[1,2,3,4] *Nigde Omer Halisdemir University, Nanotechnology Research Center, 51240, Nigde, Türkiye*
[1,4] *Nigde Omer Halisdemir University, Department of Physics, 51240, Nigde, Türkiye*
[3] *Nigde Omer Halisdemir University, Department of Mechanical Engineering, 51240, Nigde, Türkiye*

ABSTRACT

This article presents an investigation into the structural, optical, and electrical properties of Indium Tin Oxide (ITO) films that were deposited utilizing various plasma powers. The transmittance values in the visible region were measured, revealing that the ITO film deposited at 2050 W exhibited the highest transmittance (81%). Additionally, the sheet resistance values of all films were analyzed, indicating that the ITO film deposited at 2050 W had the lowest sheet resistance (64.9 Ω/sq). By means of XRD analysis, the structural properties of the films were meticulously scrutinized, and the distinctive diffraction peaks associated with the ITO films were successfully identified. Notably, the ITO film deposited at 2050 W demonstrated superior performance compared to the other films deposited using various plasma powers. Finally, we report a noteworthy efficiency of 17.03% achieved in the SHJ solar cell fabricated with the ITO film deposited at 2050 W on a 5x5 cm^2 n-type Si substrate.

Keywords: Transparent conductive oxide (TCO), Indium Tin Oxide (ITO), DC magnetron sputtering, Sheet resistance, Optical transmittance

1. INTRODUCTION

Solar energy holds significant potential as a renewable energy source, and recent advancements in technology coupled with cost reductions have made it even more promising. Various solar cells utilizing different materials have been developed, and among them, crystalline silicon (c-Si) solar cells have gained widespread use in photovoltaic (PV) technology for several decades. These c-Si solar cells offer advantages such as an optimal band gap, high efficiency, and easy access to raw materials [1]. Among the array of c-Si-based solar cell technologies, heterojunction solar cells utilizing c-Silicon (SHJ cells) have arisen as the preeminent choice in terms of efficiency. SHJ solar cells have garnered considerable interest due to their affordability, low deposition temperatures (<200°C), high efficiency, and simplified fabrication processes [2]. In recent years, remarkable conversion efficiencies of 25.6% and 26.7% have been achieved in SHJ solar cells [3], [4].

Transparent Conductive Oxide (TCO) layers play a critical role in SHJ due to their multifaceted significance and essential functionalities. These layers play a pivotal role in generating electron-hole pairs, facilitating the transmission of incoming light to the p-n junction, and minimizing reflection [5]. Furthermore, the integration of TCO layers is imperative to ensure efficient current collection in SHJ, primarily due to the elevated resistance exhibited by a-Si:H layers and the constrained lateral conductivity of p-doped a-Si:H layers. The utilization of TCO materials extends beyond the domain of SHJ and holds notable importance in a wide range of other devices, including but not limited to light-emitting diodes (LEDs) [6], dielectric transistors [7], flexible electronics [8], fuel cells [9], as well as in ubiquitous consumer electronics such as smartphones, monitors, and flat panel displays [10].

The production of TCO layers involves employing a diverse array of techniques, including but not limited to chemical vapor deposition (CVD) [11], pulsed laser deposition [12], physical vapor deposition (PVD) [13], [14], ion-assisted plasma evaporation [15], electron beam evaporation [16], direct current (DC) [17], radio frequency (RF) magnetron sputtering [18], and thermal evaporation [19]. Magnetron sputtering is a commonly employed technique in the production of TCO layers, primarily due to its favorable manufacturing characteristics. These include the ability to maintain excellent optoelectronic performance of the film [20], [21], while enabling industrial field applications through features like low substrate temperatures and high deposition rates. Furthermore, magnetron sputtering is favored for its capability to yield films with superior electrical and optical properties, as well as ensuring good surface homogeneity.

Indium tin oxide (ITO) [22], aluminum zinc oxide (AZO) [23], indium tungsten oxide (IWO) [24], indium zinc oxide (IZO) [25], and fluorine tin oxide (FTO) [26] are among the commonly employed TCOs today. ITO, specifically, is composed of a

* Corresponding author, e-mail: emrekartal4271@gmail.com (E. Kartal)
Recieved: 16.05.2023 Accepted: 25.05.2023
doi: 10.55696/ejset.1297942

solid compound consisting of indium (III) oxide (In_2O_3) and tin (IV) oxide (SnO_2), typically with a composition of 90% In_2O_3 and 10% SnO_2. Its application in solar cells is widespread due to its satisfactory conductivity and permeability performance [27]. When employed as a thin film, ITO demonstrates favorable characteristics as a viable option for a conductive layer, owing to its diminished surface resistance and enhanced permeability in comparison to alternative materials currently available. Moreover, ITO serves as an n-type semiconductor material with a discernible direct band gap spanning from 3.5 to 4.3 eV [28]. This distinctive property exerts a notable influence on the morphological, optical, and electrical attributes of ITO, consequently facilitating the fabrication of materials characterized by exceptional performance [29], [30].

In this research, a series of ITO films were deposited on 5x5 cm^2 SHJ solar cells using varying plasma powers (1800 - 1850 - 1900 - 1950 - 2000 - 2050 W), and their respective cell performances were examined. The optoelectronic characteristics of the fabricated ITO films were explored within the wavelength range of 300-1200 nm. The primary objective of this investigation was to enhance the power conversion efficiency (PCE) of SHJ solar cells by augmenting light absorption and minimizing light reflection. Subsequently, the performances of the ITO films, deposited using different plasma powers SHJ solar cells, were evaluated, resulting in the highest achieved conversion efficiency (η) of 17.03%.

2. MATERIAL AND METHOD

2.1. Thin Film Deposition

ITO films were deposited onto soda-lime glass substrates (surface: 2.5 x 2.5 cm^2, thickness: 1.1 mm) through sputtering using a DC magnetron (13.56 MHz) integrated into a PVD system. Figure 1 illustrates the schematic representation of the PVD setup. For the production of ITO films, a sputtering target with 99.999% (5N) purity of ITO was employed. The resulting films had a thickness of approximately 100 nm. Before introducing the glass substrates into the PVD chamber, a meticulous cleaning procedure was performed. Each glass substrate was subjected to a sequential cleaning regimen, involving a 5-minute immersion in acetone within an ultrasonic bath, followed by an additional 5-minute immersion in ethanol, and concluded with a 10-minute immersion in distilled water. Afterward, they were dried using Nitrogen (N_2) gas. The cleaned glass substrates were then placed within the PVD system and kept until a working pressure of $1x10^{-6}$ mbar was attained. The pressure within the PVD was maintained at $2x10^{-2}$ mbar using a continuous supply of Argon (Ar) gas and Oxygen (O_2). To prevent system contamination, an initial empty run was performed before loading the substrates into the system for the deposition process. The deposition parameters utilized for the fabrication of the ITO films are outlined in Table 1.

Table 1. Deposition parameters of ITO films.

Deposition Parameters	ITO
Base pressure (mbar)	$1x10^{-6}$
Deposition Pressure (mbar)	$2x10^{-2}$
Ar (sccm)	200
O_2 (sccm)	3.3
Temperature (°C)	200
Plasma Power (W)	1800-1850-1900-1950-2000-2050

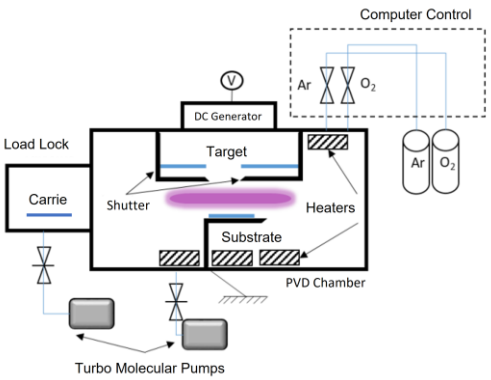

Figure 1. Schematic illustration of the PVD system.

2.2. Production of Silicon Heterojunction Solar Cells (SHJ)

In the second phase of this study, SHJ solar cells were fabricated using 5x5 cm^2, 180 µm thick, (100) orientation random pyramid textured c-Si substrates. To prepare the substrates, the oxide layer on the c-Si surface was eliminated using a hydrofluoric acid (HF) solution, followed by rinsing with distilled water and drying with N_2. Next, 10 nm thick hydrogenated amorphous silicon (a-Si:H (i)) layers were deposited on both surfaces of the c-Si substrate using the plasma-enhanced chemical vapor deposition (PECVD) method, utilizing silane (SiH_4) and hydrogen (H_2) gases. Subsequently, a 10 nm thick p-type a-Si layer (SiH_4, H_2, and Trimethyl boron (TMB) gas) was deposited on the front surface, while a 10 nm thick n-type a-Si layer (SiH_4, H_2, and Phosphine (PH_3) gas) was deposited on the back surface. On the rear surface of the n-type a-Si:H layer, consecutive layers of 40 nm ITO and 220 nm silver (Ag) were deposited using PVD. The thickness of the ITO and Ag layers was kept constant across all SHJ solar cells. For the front surface, the deposition of the ITO layer was performed on the p-type a-Si:H layer utilizing different plasma powers. Using various plasma powers, the ITO layer was deposited on the front surface of the p-type a-Si:H layer with a thickness of 100 nm. Figure 2 illustrates the fabricated SHJ solar cell structure. Ultimately, the front surface of the solar cells underwent metallization using Ag paste through the screen-printing method.

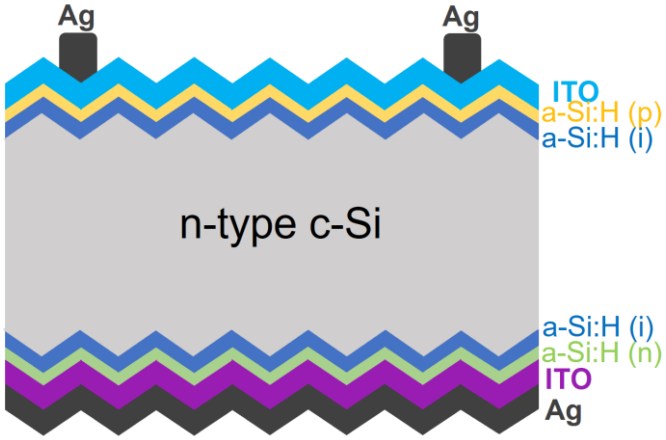

Figure 2. Schematic representation of the SHJ solar cell.

2.3. Characterization

In this study, optical, electrical, and structural parameters of ITO films were investigated. The structural properties of the ITO films were investigated using a Pan analytical-XRD device with CuKα radiation (λ=0.15418 nm) through X-ray diffraction. The determination of the thickness and optical characteristics of the thin films was carried out utilizing a Woollam V-Vase Ellipsometer, specifically within the wavelength range spanning from 300 to 1200 nm. The electrical properties of the ITO films were assessed using a contactless sheet resistance system (EddyCus® TF lab 4040 Hybrid). Furthermore, the efficiency performance of the solar cell was evaluated using the Sinton Suns-Voc WCP-120 device.

3. RESULTS AND DISCUSSION

3.1 Structural and Morphological Features

The structural properties of ITO films were investigated using X-ray diffraction method. X-ray diffraction method allows the examination of crystal structures by creating constructive and destructive interferences as a result of X-rays striking the parallel planes of atoms. In this method, the angle θ is determined for the strongest constructive interference for X-rays using Bragg's Law [31].

$$2d_{hkl}sin\theta = n\lambda \quad (1)$$

Parameters such as the distance (d) between planes of the crystal lattice, the Bragg angle (θ), an integer (n) representing the order of the diffraction peak, and the X-ray wavelength (λ) are used. Miller indices (h, k, l) of crystallographic planes are also taken into account. The calculation of the crystallite size (D) of the ITO thin films was conducted employing the Debye-Scherrer equation [32].

$$D = \frac{k\lambda}{\beta \cos\theta} \tag{2}$$

In this context, k represents the shape factor (0.9), λ the X-ray wavelength, and β the broadening of the diffraction line peak at an angle of 2θ at the full-width half-maximum (FWHM) in radians measured using the Gaussian distribution. The symbol θ represents the Bragg angle.

In this study, the XRD method was employed to analyze the crystal structure of ITO films deposited under various plasma powers (1800, 1850, 1900, 1950, 2000, and 2050 W). The scanning range for 2θ was set between 10° and 80°, and the outcomes obtained are illustrated in Figure 3. Based on the analysis results, all the deposited films exhibited polycrystalline characteristics, and the diffraction peaks (211), (222), (400), (440), and (622) indicated a cubic ITO structure (ICSD Card No. 98-005-0849) [33], [34]. The crystallinity of the ITO films was found to be influenced by the fabrication method and deposition conditions. While the films deposited at 1800 W did not exhibit (400) and (622) diffraction peaks, these peaks were observed with plasma powers exceeding 1850 W (Figure 3). This suggests that the plasma power enhances atomic arrangement, leading to an improved crystal structure. Table 2 presents the structural parameters of the ITO films deposited under different plasma powers, with these parameters calculated relative to the diffraction peak plane of highest intensity (222). According to this plane, the FWHM value of the ITO film deposited at 2050 W was determined to be the lowest (7.3E-03 rad). Conversely, the ITO film deposited at 1950 W exhibited the highest FWHM value (8.0E-03 rad). Furthermore, the 2θ values corresponding to the orientation of the ITO films (222) deposited at 1800, 1850, 1900, 1950, 2000, and 2050 W were measured as 30.21°, 30.19°, 30.22°, 29.95°, 30.21°, and 30.20°, respectively. In addition, the energy of the ions during sputtering may affect the preferred orientation of the crystalline particles because of these shifts in 2θ values. Higher sputtering powers may favor the growth of certain crystal planes, causing a shift in 2θ values [35], [36].

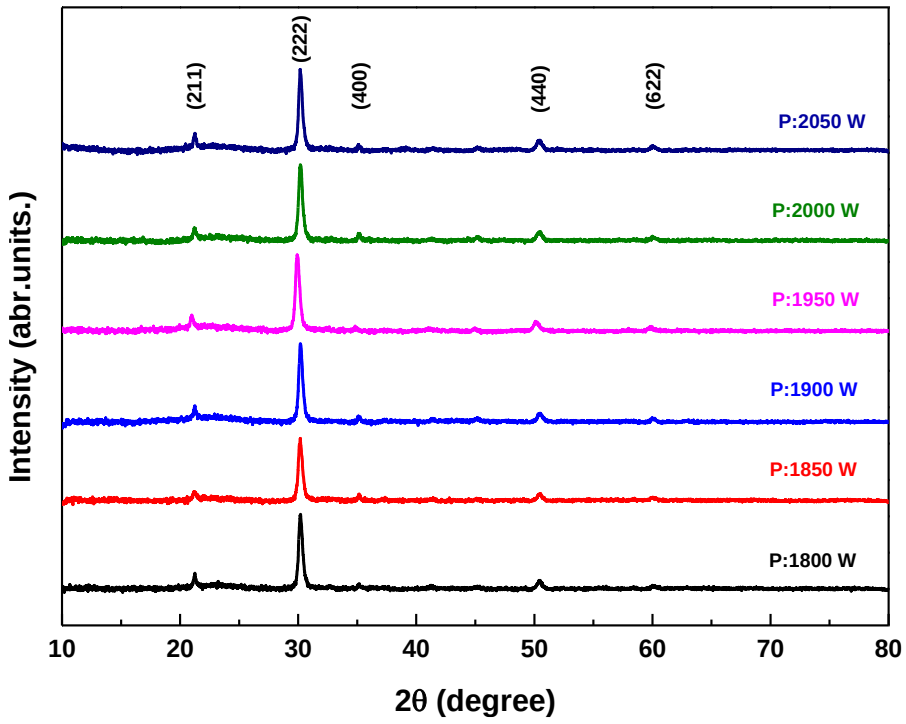

Figure 3. XRD patterns of ITO films deposited on the glass surface at 1800, 1850, 1900, 1950, 2000, and 2050 W plasma power.

The crystallite size and FWHM values of the ITO films generated under different plasma powers are presented in Table 2, and the crystallite size was determined using equation (2). A notable inverse relationship was observed between the crystallite size and FWHM values, where an increase in crystallite size corresponded to a significant decrease in FWHM (as depicted in Figure 4). Moreover, Table 2 demonstrates that the ITO films deposited at 1850 and 1950 W exhibited lower crystallite sizes (18 nm) compared to the films deposited at the same value and other plasma powers. The ITO films deposited at 1800, 1900, 2000, and 2050 W displayed the best crystallite sizes (19 nm). This outcome indicates that the ITO samples exhibit an improved crystal structure at plasma powers of 1800, 1900, 2000, and 2050 W. However, it is worth noting that the values are quite close to each other.

Table 2. FWHM (β), Bragg angle (θ), and crystallite size (D) values of ITO films deposited at 1800, 1850, 1900, 1950, 2000, and 2050 W plasma power.

Power (W)	β (rad)	θ (degres)	cosθ	D (nm)
1800	7.6E-03	15.1046	0.9655	19
1850	7.9E-03	15.0948	0.9655	18
1900	7.4E-03	15.1085	0.9654	19
1950	8.0E-03	14.9748	0.9660	18
2000	7.5E-03	15.1030	0.9655	19
2050	7.3E-03	15.1020	0.9655	19

3.2. Optical and Electrical Properties

Figures 4 and 5 depict the transmittance and reflection spectra, respectively, of the ITO films deposited on glass substrates through the PVD method, employing diverse plasma powers. A comprehensive summary of the optical properties, encompassing transmittance and reflection, of the films on the glass substrate is presented in Table 3. The transmittance spectra of the films exhibit remarkably high values within the visible region of the electromagnetic spectrum. Across the wavelength range of 400-700 nm, the ITO films deposited using different plasma powers demonstrated an average transmittance exceeding 78% and a reflectance below 18% (Table 3). Notably, the highest average transmittance of 81% was observed in the ITO film deposited at 2050 W, while the lowest transmittance was recorded in the ITO film deposited at 1800 W (77%). With an increase in plasma power, the transmittance showed an upward trend at lower wavelengths (400-700 nm), but conversely declined at higher wavelengths. Among the ITO films deposited using different plasma powers, the one with the highest transmittance within the visible region was determined to be the film generated at 2050 W, as illustrated in Figure 4.

Table 3. Transmittance, reflection and energy band gaps of ITO films deposited at 1800, 1850, 1900, 1950, 2000 and 2050 W plasma power.

Power (W)	Average Transmittance (%) (400-700 nm)	Average Reflection (%) (400-700 nm)	Eg (eV)	Transmittance (%) (550 nm)
1800	77	18	3.91	76
1850	79	18	3.91	78
1900	80	15	3.90	79
1950	79	16	3.91	79
2000	80	16	3.91	80
2050	81	15	3.91	81

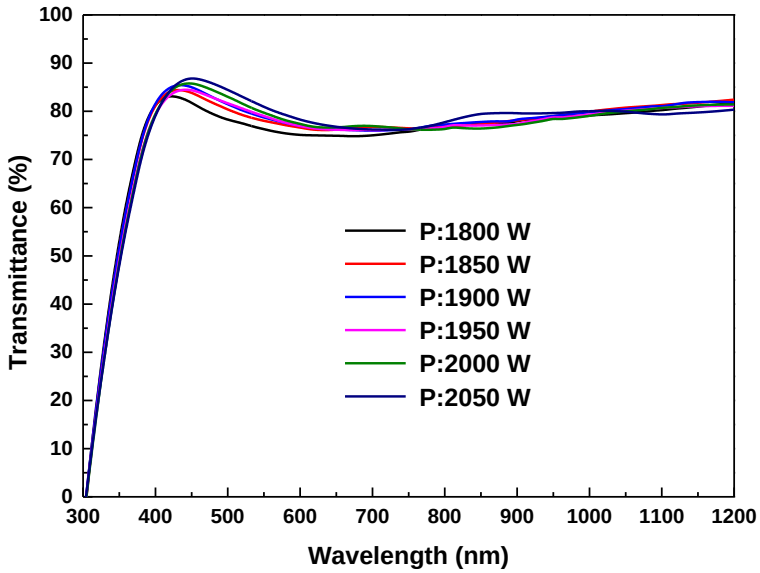

Figure 4. Transmission spectra of ITO films deposited at 1800, 1850, 1900, 1950, 2000, and 2050 W plasma power.

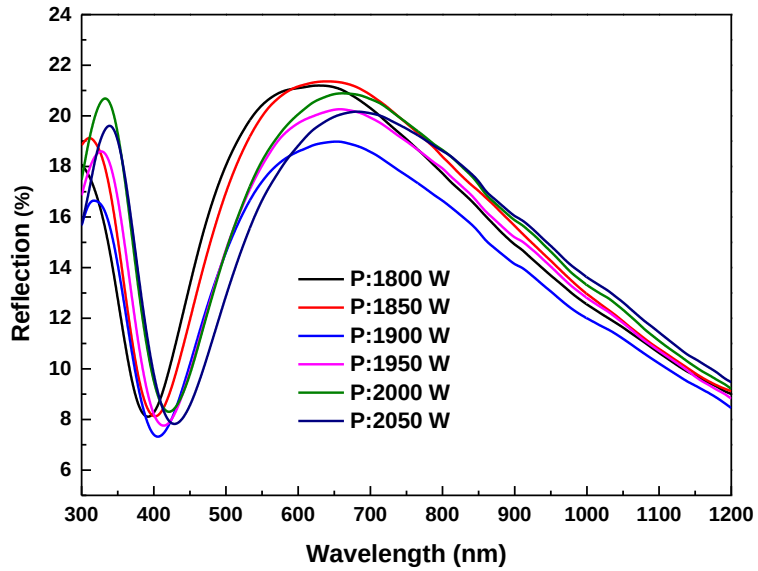

Figure 5. Reflection spectra of ITO films deposited at 1800, 1850, 1900, 1950, 2000, and 2050 W plasma power.

Figure 6 shows the graph hν corresponding to $(\alpha h\nu)^2$. The results were calculated using the bandgap measurement, Tauc plot derivative of ITO films deposited at different plasma powers [37]. The optical band gap values were determined as 3.90 eV for the film deposited at 1900 W, and as 3.91 eV for the remaining ITO films. The summary of the band gap energy values is provided in Table 3. From these findings, it can be observed that the plasma power had minimal influence on the band gap of the ITO films.

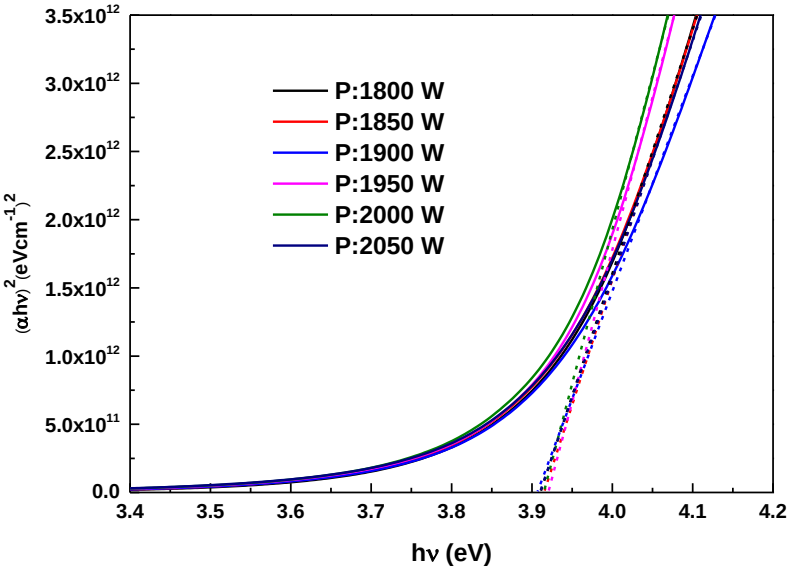

Figure 6. Graph of hν versus $(\alpha h\nu)^2$ for ITO films deposited at 1800, 1850, 1900, 1950, 2000, and 2050 W plasma power.

The transmittance values at a wavelength of 550 nm are provided in Table 3 to calculate the Figure of Merit (FOM) for ITO films deposited under different plasma powers. By utilizing the transmittance and sheet resistance properties of the ITO films at this specific wavelength, the FOM (ϕ_{TC}) values were calculated using equation (3). Figure 7 displays the obtained ϕ_{TC} and R_{sh} values for the ITO films deposited with varying plasma powers. It was observed that ϕ_{TC} values increased as the plasma power increased across all films. The ITO film deposited at 2050 W exhibited the highest FOM value of 1.87×10^{-3} Ohm $^{-1}$. Furthermore, Figure 7 also presents the R_{sh} values for the ITO films deposited under different plasma powers. The film deposited at 1800 W displayed the highest R_{sh} value of 78.7 Ω/sq, whereas the film deposited at 2050 W demonstrated the lowest R_{sh} value of 64.9 Ω/sq. It can be noted that there is a consistent decrease in R_{sh} values with the increase in plasma power. These findings indicate that the plasma power enhances the electrical properties of the material.

$$\Phi_{TC} = T^{10}/R_{sh} \tag{3}$$

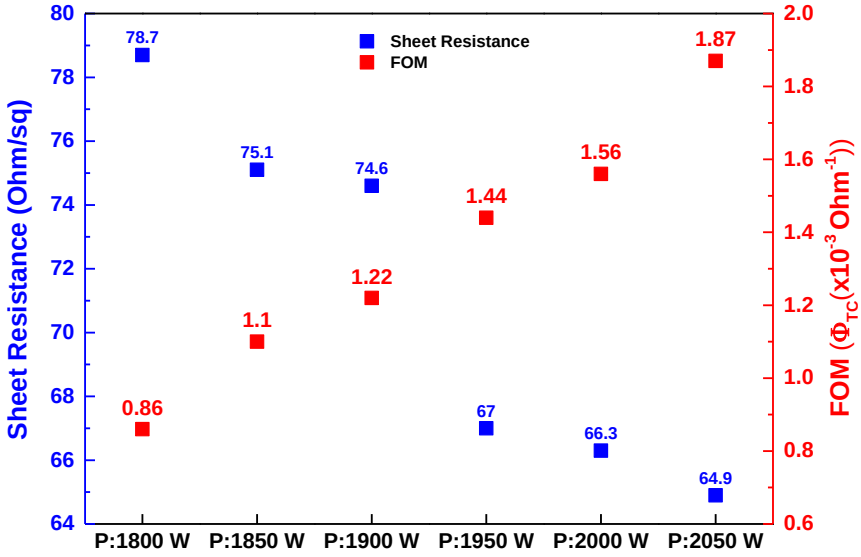

Figure 7. FOM and sheet resistance graph of ITO films deposited at 1800, 1850, 1900, 1950, 2000, and 2050 W plasma power.

The photovoltaic parameters of SHJ solar cells are provided in Table 4. Among all the plasma powers used, the ITO film deposited at 2050 W demonstrated superior performance in terms of high optical properties and low layer resistance, resulting in high efficiency. The SHJ solar cell utilizing the ITO layer deposited at 2050 W exhibited parameters of 0.613 V, 79.1%, and 17.03% for V_{OC}, FF, and η, respectively. On the other hand, the SHJ solar cell fabricated using the ITO layer deposited at 1800 W showed lower efficiency due to its lower optical properties and higher layer resistance. Increasing the plasma power resulted in higher V_{OC} and conversion efficiency in the solar cell. Figure 8 shows the current density-voltage (J-V) graph of the SHJ solar cell using ITO film deposited at 2050 W plasma power, showing its excellent performance as a TCO in the SHJ solar cell.

Table 4. Photovoltaic parameters of SHJ solar cells.

Plasma Power (W)	Voc (V)	J_{SC} (A/cm^2)	V_{MP} (V)	J_{MP} (A/cm^2)	FF (%)	Efficiency (η)
1800	0.565	0.035	0.476	0.032	77.8	15.38
1850	0.570	0.035	0.479	0.033	78.3	15.49
1900	0.587	0.035	0.497	0.032	78.6	16.14
1950	0.596	0.035	0.504	0.033	79.6	16.59
2000	0.602	0.035	0.509	0.033	78.5	16.56
2050	0.613	0.035	0.522	0.033	79.1	17.03

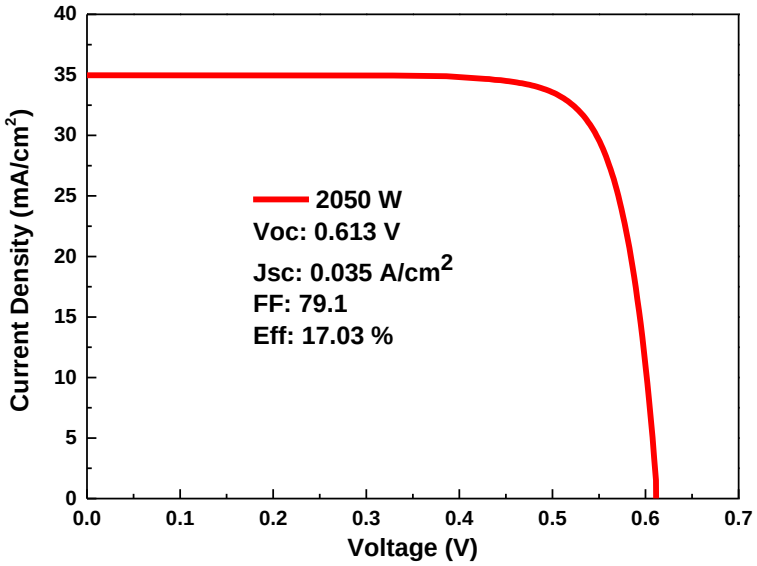

Figure 8. The current density-voltage (J-V) graph of the SHJ solar cell fabricated using ITO with a plasma power of 2050 W.

4. CONCLUSIONS

In this study, the structural, optical, and electrical properties of ITO films deposited by the DC magnetron sputtering method using different plasma powers (1800, 1850, 1900, 1950, 2000, and 2050 W) on 5x5 cm^2 n-type Si wafer at 200 °C were investigated. The optical properties were assessed by measuring the average transmittance values within the visible region (400-700 nm). The highest transmittance (81%) was observed in the ITO film deposited at 2050 W, followed by the ITO films deposited at 1900 W and 1950 W, which exhibited transmittance values of 80%. The lowest transmittance (77%) was observed in the ITO film deposited at 1800 W. The sheet resistance values were measured for all films, and the ITO film deposited at 2050 W exhibited the lowest sheet resistance (64.9 Ω/sq). Additionally, the FOM value for this film was calculated to be 1.87x10^{-3} Ohm^{-1}, indicating its superior electrical performance compared to films deposited at other plasma powers. The structural properties of the films were thoroughly examined through XRD analysis, unveiling the presence of distinct diffraction peaks corresponding to the crystal planes (211), (222), (400), (440), and (622) across all ITO films. Furthermore, the analysis revealed that the ITO films deposited at 1850 W and 1950 W exhibited crystallite sizes of 18 nm, whereas the films deposited at 1800 W,

1900 W, 2000 W, and 2050 W demonstrated crystallite sizes of 19 nm. Based on the analysis results, the ITO film deposited at 2050 W demonstrated the best overall performance among the different plasma powers. Finally, a remarkable efficiency of 17.03% was achieved in the SHJ solar cell utilizing the ITO film deposited at 2050 W.

SIMILARITY RATE: 15 %

ACKNOWLEDGEMENT

The authors gratefully acknowledge the funding from The Scientific and Technological Research Council of Turkey (TÜBITAK-20AG014).

REFERENCES

[1] C. Battaglia, A. Cuevas, and S. de Wolf, "High-efficiency crystalline silicon solar cells: status and perspectives," *Energy Environ Sci*, vol. 9, no. 5, pp. 1552–1576, 2016, doi: 10.1039/C5EE03380B.

[2] S. Q. Hussain *et al.*, "Highly transparent RF magnetron-sputtered indium tin oxide films for a-Si:H/c-Si heterojunction solar cells amorphous/crystalline silicon," *Mater Sci Semicond Process*, vol. 24, pp. 225–230, 2014, doi: https://doi.org/10.1016/j.mssp.2014.02.044.

[3] M. Taguchi, "Review—Development History of High Efficiency Silicon Heterojunction Solar Cell: From Discovery to Practical Use," *ECS Journal of Solid State Science and Technology*, vol. 10, no. 2, p. 025002, 2021, doi: 10.1149/2162-8777/abdfb6.

[4] M. A. Green, E. D. Dunlop, J. Hohl-Ebinger, M. Yoshita, N. Kopidakis, and A. W. Y. Ho-Baillie, "Solar cell efficiency tables (Version 55)," *Progress in Photovoltaics: Research and Applications*, vol. 28, no. 1, pp. 3–15, Jan. 2020, doi: https://doi.org/10.1002/pip.3228.

[5] S. de Wolf, A. Descoeudres, Z. C. Holman, and C. Ballif, "High-efficiency Silicon Heterojunction Solar Cells: A Review," *Green*, vol. 2, no. 1, pp. 7–24, 2012, doi: doi:10.1515/green-2011-0018.

[6] V. Singh, C. K. Suman, and S. Kumar, "Indium Tin Oxide (ITO) films on flexible substrates for organic light emitting diodes," in *Proc. of ASID*, 2006, p. 388.

[7] B. Walker, A. K. Pradhan, and B. Xiao, "Low temperature fabrication of high performance ZnO thin film transistors with high-k dielectrics," *Solid State Electron*, vol. 111, pp. 58–61, 2015, doi: https://doi.org/10.1016/j.sse.2015.05.004.

[8] Y. Zhang *et al.*, "Flexible transparent high-voltage diodes for energy management in wearable electronics," *Nano Energy*, vol. 40, pp. 289–299, 2017, doi: https://doi.org/10.1016/j.nanoen.2017.08.025.

[9] N. Cheng, Y. Shao, J. Liu, and X. Sun, "Electrocatalysts by atomic layer deposition for fuel cell applications," *Nano Energy*, vol. 29, pp. 220–242, 2016, doi: https://doi.org/10.1016/j.nanoen.2016.01.016.

[10] B. Yan, G. Yue, J. M. Owens, J. Yang, and S. Guha, "Light-induced metastability in hydrogenated nanocrystalline silicon solar cells," *Appl Phys Lett*, vol. 85, no. 11, pp. 1925–1927, Sep. 2004, doi: 10.1063/1.1790072.

[11] C. G. Granqvist, "Transparent conductors as solar energy materials: A panoramic review," *Solar Energy Materials and Solar Cells*, vol. 91, no. 17, pp. 1529–1598, 2007, doi: https://doi.org/10.1016/j.solmat.2007.04.031.

[12] Y.-H. Tak, K.-B. Kim, H.-G. Park, K.-H. Lee, and J.-R. Lee, "Criteria for ITO (indium–tin-oxide) thin film as the bottom electrode of an organic light emitting diode," *Thin Solid Films*, vol. 411, no. 1, pp. 12–16, 2002, doi: https://doi.org/10.1016/S0040-6090(02)00165-7.

[13] M. K. M. Ali, K. Ibrahim, O. S. Hamad, M. H. Eisa, M. G. Faraj, and F. Azhari, "Deposited indium tin oxide (ITO) thin films by dc-magnetron sputtering on polyethylene terephthalate substrate (PET)," *Rom. J. Phys*, vol. 56, no. 5–6, pp. 730–741, 2011.

[14] C. S. Moon and J. G. Han, "Low temperature synthesis of ITO thin film on polymer in Ar/H2 plasma by pulsed DC magnetron sputtering," *Thin Solid Films*, vol. 516, no. 19, pp. 6560–6564, 2008, doi: https://doi.org/10.1016/j.tsf.2007.11.028.

[15] S. Laux, N. Kaiser, A. Zöller, R. Götzelmann, H. Lauth, and H. Bernitzki, "Room-temperature deposition of indium tin oxide thin films with plasma ion-assisted evaporation," *Thin Solid Films*, vol. 335, no. 1, pp. 1–5, 1998, doi: https://doi.org/10.1016/S0040-6090(98)00861-X.

[16] D. C. Paine, T. Whitson, D. Janiac, R. Beresford, C. O. Yang, and B. Lewis, "A study of low temperature crystallization of amorphous thin film indium–tin–oxide," *J Appl Phys*, vol. 85, no. 12, pp. 8445–8450, May 1999, doi: 10.1063/1.370695.

[17] T. Karasawa and Y. Miyata, "Electrical and optical properties of indium tin oxide thin films deposited on unheated substrates by d.c. reactive sputtering," *Thin Solid Films*, vol. 223, no. 1, pp. 135–139, 1993, doi: https://doi.org/10.1016/0040-6090(93)90737-A.

[18] L. Meng and M. P. dos Santos, "Properties of indium tin oxide films prepared by rf reactive magnetron sputtering at different substrate temperature," *Thin Solid Films*, vol. 322, no. 1, pp. 56–62, 1998, doi: https://doi.org/10.1016/S0040-6090(97)00939-5.

[19] D. Raoufi, A. Kiasatpour, H. R. Fallah, and A. S. H. Rozatian, "Surface characterization and microstructure of ITO thin films at different annealing temperatures," *Appl Surf Sci*, vol. 253, no. 23, pp. 9085–9090, 2007, doi: https://doi.org/10.1016/j.apsusc.2007.05.032.

[20] L. Raniero *et al.*, "Role of hydrogen plasma on electrical and optical properties of ZGO, ITO and IZO transparent and conductive coatings," *Thin Solid Films*, vol. 511–512, pp. 295–298, 2006, doi: https://doi.org/10.1016/j.tsf.2005.12.057.

[21] S. M. Kim, H.-W. Choi, K.-H. Kim, S.-J. Park, and H.-H. Yoon, "Preparation of ITO and IZO thin films by using the facing targets sputtering (FTS) method," *J. Korean Phys. Soc*, vol. 55, no. 5, pp. 1996–2001, 2009, [Online]. Available: http://dx.doi.org/10.3938/jkps.55.1996

[22] T. J. Burke and C. Segrin, "Examining Diet- and Exercise-Related Communication in Romantic Relationships: Associations With Health Behaviors," *Health Commun*, vol. 29, no. 9, pp. 877–887, Oct. 2014, doi: 10.1080/10410236.2013.811625.

[23] J. Montero, C. Guillén, and J. Herrero, "AZO/ATO double-layered transparent conducting electrode: A thermal stability study," *Thin Solid Films*, vol. 519, no. 21, pp. 7564–7567, 2011, doi: https://doi.org/10.1016/j.tsf.2010.12.103.

[24] H. Park, J. Lee, H. Kim, D. Kim, J. Raja, and J. Yi, "Influence of SnO2:F/ZnO:Al bi-layer as a front electrode on the properties of p-i-n amorphous silicon based thin film solar cells," *Appl Phys Lett*, vol. 102, no. 19, p. 191602, May 2013, doi: 10.1063/1.4807127.

[25] M. P. Taylor *et al.*, "The Remarkable Thermal Stability of Amorphous In-Zn-O Transparent Conductors," *Adv Funct Mater*, vol. 18, no. 20, pp. 3169–3178, Oct. 2008, doi: https://doi.org/10.1002/adfm.200700604.

[26] R. Riveros, E. Romero, and G. Gordillo, "Synthesis and characterization of highly transparent and conductive SnO2: F and In2O3: Sn thin films deposited by spray pyrolysis," *Brazilian journal of physics*, vol. 36, pp. 1042–1045, 2006.

[27] A. Ambrosini, A. Duarte, K. R. Poeppelmeier, M. Lane, C. R. Kannewurf, and T. O. Mason, "Electrical, Optical, and Structural Properties of Tin-Doped In2O3–M2O3 Solid Solutions (M=Y, Sc)," *J Solid State Chem*, vol. 153, no. 1, pp. 41–47, 2000, doi: https://doi.org/10.1006/jssc.2000.8737.

[28] J. M. Gaskell and D. W. Sheel, "Deposition of indium tin oxide by atmospheric pressure chemical vapour deposition," *Thin Solid Films*, vol. 520, no. 12, pp. 4110–4113, 2012, doi: https://doi.org/10.1016/j.tsf.2011.04.191.

[29] M. J. Alam and D. C. Cameron, "Optical and electrical properties of transparent conductive ITO thin films deposited by sol–gel process," *Thin Solid Films*, vol. 377–378, pp. 455–459, 2000, doi: https://doi.org/10.1016/S0040-6090(00)01369-9.

[30] A. H. Sofi, M. A. Shah, and K. Asokan, "Structural, Optical and Electrical Properties of ITO Thin Films," *J Electron Mater*, vol. 47, no. 2, pp. 1344–1352, 2018, doi: 10.1007/s11664-017-5915-9.

[31] D.-W. Kim and D.-W. Park, "Preparation of indium tin oxide (ITO) nanoparticles by DC arc plasma," *Surf Coat Technol*, vol. 205, pp. S201–S205, 2010, doi: https://doi.org/10.1016/j.surfcoat.2010.07.078.

[32] A. H. Sofi and M. A. Shah, "Structural and electrical properties of copper doped In2O3 nanostructures prepared by citrate gel processes," *Mater Res Express*, vol. 6, no. 4, p. 045039, 2019, doi: 10.1088/2053-1591/aafc0b.

[33] S.-Y. Lien, "Characterization and optimization of ITO thin films for application in heterojunction silicon solar cells," *Thin Solid Films*, vol. 518, no. 21, Supplement, pp. S10–S13, 2010, doi: https://doi.org/10.1016/j.tsf.2010.03.023.

[34] T. Ogi, D. Hidayat, F. Iskandar, A. Purwanto, and K. Okuyama, "Direct synthesis of highly crystalline transparent conducting oxide nanoparticles by low pressure spray pyrolysis," *Advanced Powder Technology*, vol. 20, no. 2, pp. 203–209, 2009, doi: https://doi.org/10.1016/j.apt.2008.09.002.

[35] W.-F. Wu, B.-S. Chiou, and S.-T. Hsieh, “Effect of sputtering power on the structural and optical properties of RF magnetron sputtered ITO films,” vol. 9, no. 6, pp. 1242–1249, Jun. 1994, doi: https://doi.org/10.1088/0268-1242/9/6/014.

[36] A. Mansingh and V. Kumar, “Properties of RF-sputtered ITO films on substrates above and below the virtual source,” vol. 22, no. 3, pp. 455–457, Mar. 1989, doi: https://doi.org/10.1088/0022-3727/22/3/013.

[37] Tauc, "Optical properties and electronic structure of amorphous Ge and Si," Materials research bulletin, vol. 3, no. 1 second. 37-46, 1968, doi: https://doi.org/10.1016/0025-5408(68)90023-8

Eurasian Journal of Science Engineering and Technology

Research Article

LARGE-SCALE SYNTHESIS OF HOMOGENEOUS WS_2 FILMS BY PHYSICAL VAPOR DEPOSITION

Ali ALTUNTEPE[1],*, Serkan ERKAN[2], Güldöne KARADENİZ[3]

[1,2,3] *Nigde Omer Halisdemir University, Nanotechnology Research and Application Center, 51240, Niğde, Türkiye*

ABSTRACT

TMDs are semiconductors, unlike graphene, and have a direct bandgap when converted from bulk to thin film. This property makes TMDs an ideal material for optoelectronic and photovoltaic applications due to their strong optical absorption and photoluminescence effect. The WS_2, a popular TMD, has unique properties such as low friction coefficient, high thermal stability, and good electrical conductivity, and a bandgap energy of approximately 1.2 eV and 2.2 eV for indirect and direct behaviors. The article also discusses various methods for synthesizing WS_2, including chemical vapor deposition (CVD), physical vapor deposition (PVD), hydrothermal synthesis, and solvothermal synthesis. PVD is a scalable method for producing large-area films and coatings with high quality, but the difficulty of controlling the sulfur or selenium sources in this method leads to the need for optimizing growth parameters for large-scale and high-quality WS_2 film synthesis. The study reports the successful growth of large-scale and homogeneous WS_2 films on a glass substrate using PVD and optimized substrate temperature. The results of this study provide valuable information for the advancement of WS_2 film growth techniques and the development of WS_2-based semiconductor technologies, such as transistors, diodes, photodetectors, and solar cells.

Keywords: WS_2, PVD, Substrate temperature

1. INTRODUCTION

Since the isolation of graphene, the first 2D material with superior electrical, chemical and mechanical properties, interest in the synthesis, characterization and application of graphene and other 2D materials has rapidly increased [1, 2]. The outstanding optical properties like light transmittance and energy band gap of graphene and 2Ds, and in particular those of TMDs, have been promising for the use of these materials in energy and photovoltaic applications, and studies in this field have intensified [3]. The TMDs known to have MX_2 (M: Mo, W; X: S, Se, Te) structure are semiconductors in contrast to the semi-metal nature of graphene and when they are converted from bulk form to thin film, the indirect band gap becomes direct band gap [4]. This transition leads to a strong optical absorption by creating a large photoluminescence effect in the material which is one of the main reasons why TMDs are preferred for optoelectronic and photovoltaic applications. The estimated about 10% absorbance value of monolayer TMDs in the visible region corresponds to 50 nm thick silicon commonly used in solar cell applications. However, while it can produce 2.0−4.5 mA/cm^2 photocurrent, this value is limited to about 0.1 mA/cm^2 for the silicon of approximately similar thickness [5]. In addition, TMDs have been prominent and popular thanks to their band gap energy, which can be modified by doping and adjusted to a desired level. This has paved the way for TMDs to be used in many semiconductor technologies such as transistors, diodes, photodetectors, and solar cells [6].

The WS_2 is one of the most popular 2D materials in among TMDS because of it has attractive properties. The WS_2 has a layered structure, with each layer consisting of a sheet of tungsten atoms sandwiched between two layers of sulfur atoms. The layers are held together by weak Van der Waals forces. This layered structure gives WS_2 its unique properties such as its low friction coefficient, high thermal stability, and good electrical conductivity. The WS2 material has an approximately 1.2 eV and 2.2 eV band gap for indirect and direct behaviors, and a mobility value of about 150 $cm^2\ V^{-1}\ s^{-1}$ has an n-type property [7]. The WX_2 group, has the lowest bandwidth among TMDs with a 1.1 eV bandwidth [8]. Moreover, its having p-type features allows homo and hetero PN junction structures to be obtained. More specifically, the mentioned TMDs' property regarding having different band gap values enables the development of open circuit voltage (Voc), which is an important parameter in solar cell applications. WS_2 can be synthesized using several methods, including chemical vapor deposition (CVD), physical vapor deposition (PVD) hydrothermal synthesis, mechanical exfoliation, solvothermal synthesis, and sulfurization of tungsten [2]. PVD is a versatile and scalable method that can produce large-area films and coatings with high quality [9]. Hydrothermal synthesis and solvothermal synthesis are relatively simple and low-cost methods but typically result in lower-quality WS_2 compared to PVD. Although PVD method provide large area film growth difficulty of controlling S or Se sources in this method [10]. Therefore, growth parameters should be optimized to homogeny and high quality WS_2 films growth.

* Corresponding author, e-mail: altuntepeali@gmail.com (A. Altuntepe)
Recieved: 24.05.2023 Accepted: 09.06.2023
doi: 10.55696/ejset.1301601

In this study, large scale and homogeneous WS_2 films were growth. The WS_2 films were growth on the glass substrate with the PVD system and by optimizing the substrate temperature of RT, 300 °C, 400 °C, and 500 °C. Optimum substrate temperature was determined to obtain large scale and high quality WS_2 film synthesis. The results of the study provide valuable information for the development and improvement of WS_2 film growth techniques, which can ultimately lead to the advancement of the technology.

2. MATERIAL AND METHOD

In this study, we investigated substrate temperature effect on the WS_2 growth by PVD (RF sputtering) methods. All growth processes were given in Table 1. For this aim, glass used as a substrate and cleaning processes applied to substrate before growth process. First of all, all substrates were cleaned with Acetone, IPA, and DW with 10 min, 10 min, and 20 min in the ultrasonic bath, respectively. After this, all substrates were dried with N_2 gas flow. The ultrasonic plasma cleaner was used at last step of the cleaning process for removed remaining contaminants. The magnetron sputtering was carried out at 15 nm film thickness with RF power of 50 Watt at a sputtering base pressure of $1.6x10^{-6}$ Torr and growth pressure of $3x10^{-3}$ Torr in a pure Ar gas atmosphere. The 15 nm thick WS_2 films coated by RF sputtering method at room temperature (RT), 300 °C, 400 °C and 500 °C substrate temperature with deposition rate of 0.2 Å/s.

Table 1. Cleaning and growth process of WS_2

Cleaning Process		**Growth Process**	
Acetone	10 min.	**Base Pressure**	$1.6x10^{-6}$ Torr
IPA	10 min.	**Growth Pressure**	$3x10^{-3}$ Torr
DW	20 min.	**RF Power**	50 Watt
Dried	Ar gas	**Deposition Rate**	0.2 Å/s
Ultrasonic Plasma Cleaner	20 min.	**Temperature**	RT, 300 °C, 400 °C, 500 °C

The structural properties of WS_2 films were characterized by Raman spectra and scanning electron microscope (SEM) measurements. In addition, the optical properties were determined with ellipsometer and photoluminescence spectroscopy (PL).

3. RESULTS AND DISCUSSION

The Raman spectra of 2D WS_2 films grown at RT, 300, 400 and 500 °C substrate temperature and exposed to a 532 nm laser are shown in Figure 1. The first-order Raman modes of WS_2 films at the Brillouin zone center were attributed to E_{2g}^1 and A_{1g} modes. The E_{2g}^1 mode corresponds to the transversal movement of W and S atoms in the lattice, while the A_{1g} mode corresponds to the longitudinal movement of these atoms. In addition, the longitudinal acoustic phonons 2LA(M), which denote in-plane collective movements of atoms in the WS_2 lattice, and other WS_2 modes were labeled in the graph. The E_{2g}^1 and A_{1g} modes were observed at approximately 354 cm^{-1} and 418 cm^{-1} for RT, 300 °C and 400 °C substrate temperatures. However, the E_{2g}^1 mode was not observed for 500 °C. This indicates that the 2LA(M) and E_{2g}^1 modes overlapped at approximately 352 cm^{-1}, and the A_{1g} mode was detected at around 418 cm^{-1}. Furthermore, at a 400 °C substrate temperature, the 2LA(M) and E_{2g}^1 mode overlapped at approximately 354 cm^{-1}. The intensity of the LA(M) increased while that of the A_{1g} decreased with a reduction in the number of layers of 2D-WS_2 films. The Raman spectra showed that the 400 °C sample tended to grow as a few layers, while the other samples exhibited multi-layer or bulk behavior.

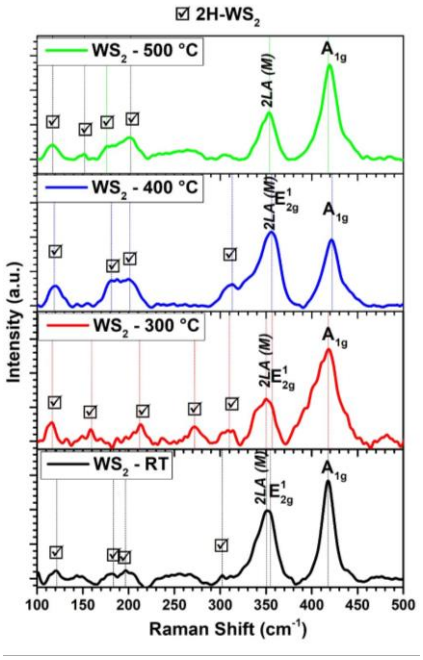

Figure 1. Raman spectra of 2D-WS_2 films growth with RT, 300, 400, and 500 °C substrate temperature

The PL measurements of 2D-WS_2 grown at RT, 300°C, 400°C and 500°C substrate temperature are shown in Figure 2. The bulk WS_2 exhibits PL emission at around 1.2 eV as an indirect band transition in the literature [11]. In Figure 2, the sample of RT, 300 °C, and 500 °C substrate temperature showed approximately 1.25 eV PL emission that situation attributed to the indirect band transition. The statement indicates that the photoluminescence (PL) intensity of bulk samples is very weak. This finding is in line with the behavior of an indirect bandgap semiconductor in its bulk form. An indirect bandgap material has a lower efficiency in emitting light compared to a direct bandgap material. Therefore, the weak PL intensity observed in bulk samples suggests that the emission of light is less efficient due to the indirect bandgap nature of the semiconductor material [12]. The WS_2 films grown from 400 °C substrate temperature was observed three PL emissions at 1.25 eV, 1.78 eV and 1.93 eV. The PL emissions at 1.78 eV and 1.93 eV which are associated with the B and A excitons were attributed to the direct band transitions [13].

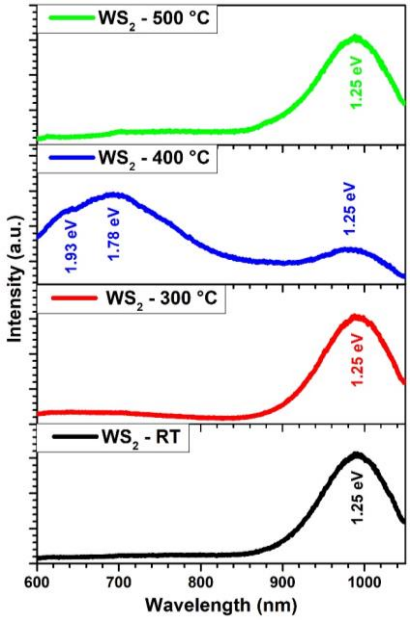

Figure 2. PL spectra of 2D-WS_2

Optical transmission data of 2D-WS_2 films are shown in Figure 3. In Figure 3, the average optical transmission of 2D-WS_2 films in the visible range (400-800 nm) is determined to be 64%, 65%, 78% and 64% for the substrate temperature of RT, 300, 400 and 500 °C respectively. For WS_2 films grown at a substrate temperature of 400°C, the optical transmission indicated a few layers of WS_2 film [14].

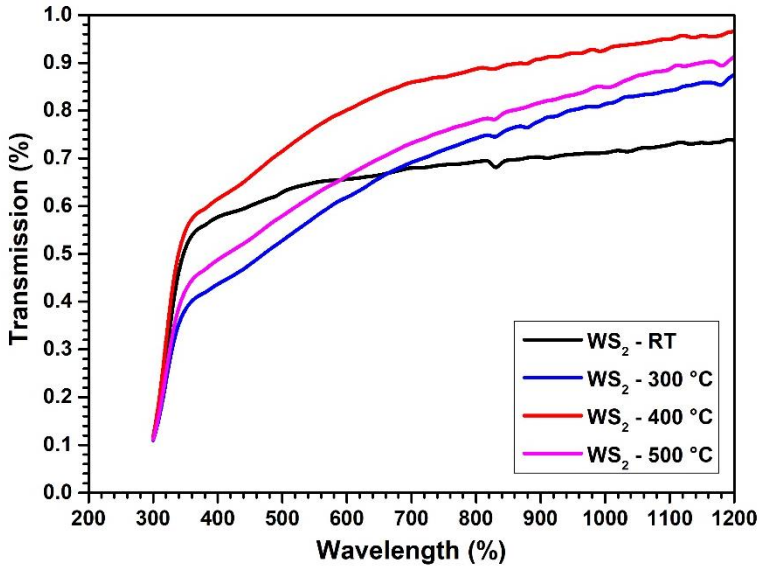

Figure 3. Optical transmission of 2D-WS_2 films

The band gap is an important characteristic of semiconductors, and it determines their electrical and optical properties. The optical properties of the 2D-WS_2 films growth on glass substrate were determined by using the bandgap values calculated from the absorption coefficient obtained by the transmittance spectra of the samples. The bandgap energy values of the samples were calculated by measuring the transmittance spectra with an ellipsometer (J.A. Woollam-VASE) system in our research center. The absorption coefficients of the samples were calculated using the Lambert-Beer law [15] with the measured transmittance values at room temperature in the range of 200-1200 nm and the thicknesses of the WS_2 films.

$$\alpha = \frac{1}{d}\ln\frac{1}{T} \quad (1)$$

The absorption coefficient (α) in Equation (1) represents the absorption coefficient, d represents the thickness of the sample, and T represents the optical transmittance. Using the calculated absorption coefficients with Equation (1), the bandgap energy values of the 2D-WS_2 films were calculated using Equation (2), where E_g is the bandgap energy, A is the constant, hv is the photon energy, and n is the nature of the transition, which takes the value of 1/2 for direct bandgap semiconductors [16].

$$(\alpha hv)^2 = A(hv - E_g) \quad (2)$$

The $(\alpha hv)^2$ - (hv) graph of the samples was plotted (Figure 4) using Equation (2), and the bandgap of the 2D-WS_2 films was determined by identifying the point where the linear part of the curve intersects the hv axis. In the Figure 4, the band gap of the 2D-WS_2 films were determined as 1.85 eV, 2.00 eV, 2.20 eV, and 2.07 eV for RT, 300 °C, 400 °C, and 500 °C substrate temperatures, respectively. In the case of 2D-WS_2 films, the band gap has been reported to be around 2.25 eV for direct band behavior in the literature [12]. It is important to note that the band gap can be affected by various parameters, such as the substrate temperature during growth. In this context, it has been observed that the sample grown at a substrate temperature of 400 °C tends to direct band behavior, whereas the other samples exhibit indirect behaviors.

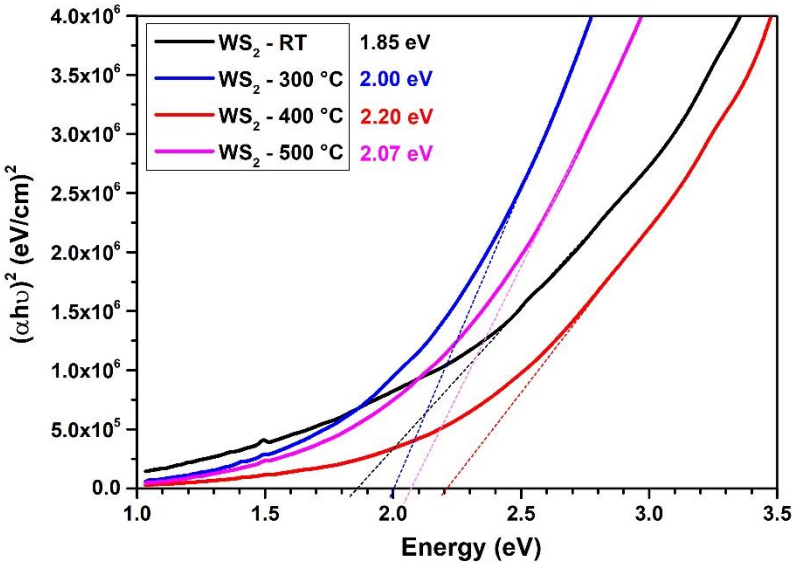

Figure 4. Optical band gap of 2D-WS_2 films.

4. CONCLUSION

In the present study, WS_2 films were grown by PVD method. The different substrate temperatures were considered and 400 °C substrate temperature was determined as the optimum WS_2 growth temperature. According to the Raman and PL spectroscopy measurements of WS_2 films, RT was found to be insufficient for the formation of single phase WS_2 as the obtained film showed bulk structure. With the increase of the substrate temperature, the bulk structure changed into the multilayer structure and the indirect band transition evolved into a direct band transition. Therefore, we conclude that the substrate temperature is highly effective to synthesize high quality WS_2 films by 15 nm WS_2 film at 400 °C. These results enable the use of WS_2 films in optoelectronic applications.

SIMILARITY RATE: 13%

AUTHOR CONTRIBUTION

Ali ALTUNTEPE: Conceptualization, methodology, data curation, writing, editing etc.
Serkan ERKAN: Conceptualization, methodology, data curation, writing, editing etc.
Güldöne KARADENİZ: Characterization.

CONFLICT of INTEREST

The authors declared that they have no known conflict of interest.

REFERENCES

[1] A. Altuntepe *et al.*, "Hybrid transparent conductive electrode structure for solar cell application," vol. 180, pp. 178-185, 2021.
[2] C. Feng, L. Huang, Z. Guo, and H. J. E. c. Liu, "Synthesis of tungsten disulfide (WS2) nanoflakes for lithium ion battery application," vol. 9, no. 1, pp. 119-122, 2007.
[3] B. Luo, G. Liu, and L. J. N. Wang, "Recent advances in 2D materials for photocatalysis," vol. 8, no. 13, pp. 6904-6920, 2016.

[4] S. Tanwar, A. Arya, A. Gaur, and A. J. J. o. P. C. M. Sharma, "Transition metal dichalcogenide (TMDs) electrodes for supercapacitors: a comprehensive review," vol. 33, no. 30, p. 303002, 2021.
[5] C. Cong, J. Shang, Y. Wang, and T. J. A. O. M. Yu, "Optical properties of 2D semiconductor WS2," vol. 6, no. 1, p. 1700767, 2018.
[6] M. Donarelli and L. J. S. Ottaviano, "2D materials for gas sensing applications: a review on graphene oxide, MoS2, WS2 and phosphorene," vol. 18, no. 11, p. 3638, 2018.
[7] C. Lan, C. Li, J. C. Ho, and Y. J. A. E. M. Liu, "2D WS2: from vapor phase synthesis to device applications," vol. 7, no. 7, p. 2000688, 2021.
[8] H. Shi, H. Pan, Y.-W. Zhang, and B. I. J. P. R. B. Yakobson, "Quasiparticle band structures and optical properties of strained monolayer MoS 2 and WS 2," vol. 87, no. 15, p. 155304, 2013.
[9] R. Zan, M. A. Olgar, A. Altuntepe, A. Seyhan, and R. J. R. E. Turan, "Integration of graphene with GZO as TCO layer and its impact on solar cell performance," vol. 181, pp. 1317-1324, 2022.
[10] L. Li, R. Long, and O. V. Prezhdo, "Why chemical vapor deposition grown MoS2 samples outperform physical vapor deposition samples: time-domain ab initio analysis," *Nano letters*, vol. 18, no. 6, pp. 4008-4014, 2018.
[11] M. K. S. Bin Rafiq *et al.*, "WS2: a new window layer material for solar cell application," *Scientific reports*, vol. 10, no. 1, p. 771, 2020.
[12] H. Zeng *et al.*, "Optical signature of symmetry variations and spin-valley coupling in atomically thin tungsten dichalcogenides," vol. 3, no. 1, p. 1608, 2013.
[13] Y. Gao *et al.*, "Large-area synthesis of high-quality and uniform monolayer WS2 on reusable Au foils," *Nature communications*, vol. 6, no. 1, p. 8569, 2015.
[14] Y. Niu *et al.*, "Thickness-dependent differential reflectance spectra of monolayer and few-layer MoS2, MoSe2, WS2 and WSe2," *Nanomaterials*, vol. 8, no. 9, p. 725, 2018.
[15] J. I. Pankove, *Optical processes in semiconductors*. Courier Corporation, 1975.
[16] J. Tauc, "Optical properties and electronic structure of amorphous Ge and Si," *Materials Research Bulletin*, vol. 3, no. 1, pp. 37-46, 1968.